published in *Journal of Geophysical Research*, Vol. 105, No. E8, pages 20,307 – 20,331, August 25, 2000
Copyright 2000 American Geophysical Union. Further electronic distribution is not allowed

Thorium abundances on the lunar surface

D. J. Lawrence[1], W. C. Feldman[1], B. L. Barraclough[1], A. B. Binder[2], R. C. Elphic[1], S. Maurice[3], M. C. Miller[4], and T. H. Prettyman[1]

Abstract. Measurements of absolute thorium abundances on the lunar surface are presented using both the high- and low-altitude data taken with the Lunar Prospector Gamma-Ray Spectrometer. An analysis of the uncertainties shows that the measured uncertainties are < 0.5 μg/g and are close to the theoretical limit of Poisson statistics. Currently, the overall systematic uncertainties are likely dominated by variations in background counts. The relative systematic uncertainties are thought to be no larger than 30% for the high-altitude data and 15% for the low-altitude data. A comparison of high- and low-altitude data show that most regions having thorium abundances > 7 μg/g are likely small area regions ≤ $(150\ \mathrm{km})^2$. Using lunar topographic data, we have shown that the thorium abundances in the lunar highlands and portions of South Pole-Aitken (SPA) Basin are larger for lower elevations. We have also studied a number of regions with anomalously high thorium abundances such as the northwestern region of SPA Basin, the crater Arago in western Tranquillitatis, and the Compton/Belkovich region in the northeastern highlands. The Compton/Belkovich region appears to be enriched with evolved rocks such as alkali anorthosite and currently represents the only such extended region on the Moon that has been identified. In contrast, Tycho crater has very low thorium abundances which suggests that KREEP was not assimilated at depth in this portion of the Moon.

1. Introduction

Thorium is a key element for tracing the history and evolution of the Moon and the lunar surface because it is enriched in a material called KREEP [potassium (K), rare earth elements (REE), phosphorus (P)] which is thought to have formed between the lunar crust and mantle. Specifically, it is thought that as the Moon cooled and minerals crystallized from a magma ocean, dense minerals sank to form the mantle and light minerals floated to the surface to form the crust. The last material to crystallize was rich in elements that do not substitute easily into the crystal lattice of the major rock-forming minerals (e.g., Th, K, and REE). Detailed explanations of how KREEP relates to lunar formation and evolution can be found in many references and are therefore not discussed here [e.g., *Vaniman et al*., 1991; *Warren and Wasson*, 1979; *Warren*, 1985, and references therein]. In this paper, we present and describe the most recent thorium abundance data obtained with the Lunar Prospector (LP) Gamma-Ray Spectrometer (GRS). A rigorous determination of the absolute thorium abundance from LP GRS data requires that detailed detector modeling and spectral fitting analyses be carried out. However, because the 2.61-MeV γ-ray line produced by ^{232}Th is very strong, has few competing γ-ray lines in its energy range, and shows large variations over the lunar surface, it is possible to obtain estimates of relative and absolute thorium abundances by simply measuring γ-ray counting rates within an energy window surrounding the 2.61-MeV line. Preliminary results of this window counting rate technique are described by *Lawrence et al*. [1998, 1999a]. A number of key results have been discovered regarding the abundance of thorium on the lunar surface using this technique. These results include the following:

1. The highest thorium abundances on the Moon are located around the Imbrium basin region. The locations of high-thorium abundances are associated with craters and highlands regions, some of which may be related to Imbrium ejecta and/or post-Imbrium KREEP volcanism. In particular, the regions with the highest thorium abundances are near Aristillus crater, Aristarchus crater, Mairan crater, Kepler crater, the Fra Mauro region near the Apollo 14 landing site, the Apennine bench region near the Apollo 15 landing site, and the highlands regions north and northwest of Imbrium basin.
2. The mare basalt within Imbrium basin has distinctly lower thorium abundances than many of the surrounding regions but has higher thorium abundances than the eastern mare basalt regions.
3. South Pole-Aitken (SPA) Basin has moderately high thorium abundances compared to the surrounding highlands. In addition, the locations within SPA having the highest thorium abundances do not appear to be areas with extensive mare basalt, in contrast to the expectation of *Hawke and Spudis* [1980].
4. There exists a moderately high thorium region in the lunar highlands (60°N, 100°E) which has a small spatial size (150 – 300 km diameter). While high in thorium compared to the surrounding highlands, this region does not have any other abundance anomalies as determined by the Clementine spectral reflectance (CSR) measurements of *Lucey et al*. [this issue].
5. The measured distribution of thorium abundances closely matches the distribution of samarium and gado-

linium abundances inferred from combined LP neutron spectrometer and CSR data [*Elphic et al*., 1998, this issue].

Here we expand on the previous studies by describing the absolute thorium abundance measurements in more detail. Specifically, thorium abundance measurements have been derived from both high- and low-altitude data. Since the LP GRS is an uncollimated, omnidirectional γ-ray detector, the measured surface resolution is a direct function of the spacecraft height above the lunar surface. The surface resolution (full-width, half maximum) of the low-altitude data (mean spacecraft height: 32 km; see Table 1) is ~(45 km)^2, which is three times smaller than the surface resolution of the high-altitude data (mean spacecraft height: 100 km) of ~(150 km)^2. See *Reedy et al*. [1973] for a general discussion of the surface resolution that can be obtained with planetary gamma-ray spectroscopy. In the initial study of *Lawrence et al*. [1998] we presented relative thorium abundances using the high-altitude data on 5° x 5° (150 x 150 km) equal area pixels. The first whole-Moon measurements of absolute thorium abundances were presented by *Lawrence et al.* [1999a] using the low-altitude thorium data on 2° x 2° (60 x 60 km) equal area pixels. Here we present together both high- and low-altitude measurements of absolute thorium abundances measured on 60 x 60 km equal area pixels. Note that while the high-altitude data in this paper are presented on 60 x 60 km pixels, the surface resolution of the high-altitude measurements is still ~(150 km)^2. In addition, the calculated gamma-ray flux per unit thorium abundance has been revised in this paper (see section 3) so that the low-altitude thorium abundances are ~25% higher than the abundances presented by *Lawrence et al*. [1999a]. In this paper, we describe in detail the abundance uncertainties associated with the window counting rate method of calculating absolute abundances. Next, we discuss the global thorium data and examine the similarities and differences between the high- and low-altitude data. We then examine relationships between the global thorium data and other global data sets. Finally, we describe thorium abundances for a number of locations on the Moon using the low-altitude thorium data.

2. LP GRS Data Sets

The LP thorium data are divided into two major data sets. A summary of the data sets is given in Table 1. A set of high-altitude data (mean spacecraft height: 100 km) was measured from January 16, 1998, to December 19, 1998, and a set of low-altitude data (mean spacecraft height: 32 km) was measured from December 19, 1998, to July 31, 1999. On October 6 – 8, 1998, the spin axis of the LP spacecraft was flipped from pointing toward the ecliptic north to the ecliptic south. Since the response of the GRS is asymmetric with respect to lunar latitude and spacecraft spin axis orientation [*Lawrence et al.*, 1998; *Feldman et al.*, 1999], the high-altitude data were subdivided into two data sets corresponding to the two different spin axis orientations. The two high-altitude data sets were combined into the single set of high-altitude data shown in Table 1 after making an ~2% count rate offset correction to the spin axis south data.

GRS spectra were collected in time increments of 32s, during which time the spacecraft covered a ground track distance of roughly 50 km. To create a composition map, each spectrum is assigned to one of 11,306 approximately equal area (60 x 60 km) pixels on the basis of instantaneous position of the spacecraft halfway through each data collection cycle. Currently, no corrections have been made to account for spacecraft motion during the data collection cycle. Table 1 shows the total number of 32s spectra collected for each data set. Out of a possible 562 days of data collection, 13.7% (high-altitude) and 13.1% (low-altitude) of the data have been lost or are unusable for elemental mapping. Sources of loss include incomplete Deep Space Network coverage, bad data sync words and/or check sums, spacecraft maneuvers, and solar energetic particle events, which saturate the GRS detector with very high background counting rates. The average number of measured spectra per 60 x 60 km pixel is also listed in Table 1 for the latitudes ±90°, ±45°, and 0°. Because LP was in a polar orbit, there were over 30 times more spectra collected per unit area at the poles than at the equator.

As explained elsewhere [*Lawrence et al*., 1998, 1999a, b], various time-dependent corrections have been made to the raw GRS counting rate data. These include corrections for gain variations in the GRS detector, dead time counting rate variations, counting rate variations due to the changing flux of galactic cosmic rays hitting the Moon (which affects the time-dependent background under the thorium γ-ray line), and variations in the solid angle subtended by the Moon due to the varying heights of the LP spacecraft. As part of the solid angle corrections, both the high- and low-altitude data sets were normalized to a spacecraft altitude of 100 km to enable easy comparisons between the data sets. Finally, corrections have also been made for variations due to the asymmetric response of the GRS for different latitudes.

3. Uncertainties in the Measured Thorium Abundances

Thorium abundances are derived by measuring the counting rate of the 2.61-MeV γ-ray line produced by radioactive decay of ^{232}Th. Because of the reasons listed in section 1, estimates of absolute thorium abundances can be calculated by making the following assumptions: (1) Assume that the continuum background counts and non-thorium discrete line γ-ray counts within the 2.5- to 2.7-MeV window are constant over the Moon. (2) Define the pixel with the minimum window counting rate to have a thorium abundance of 0 μg/g. (3) Since we are making a cosmic ray correction to the entire count rate within the 2.5- to 2.7-MeV window, this analysis assumes that varia-

tions in cosmic ray input have a zero average for each 60 x 60 km pixel. Assumption 2 probably does not hold in a strict sense because the lowest thorium abundances on the Moon are likely around 0.4±0.2 μg/g as measured from lunar highlands meteorites [*Korotev*, 1999]. However, since 0.4 μg/g is comparable to some of the measured and/or estimated uncertainties (see below), to a first approximation, it is reasonable to use assumption 2. The minimum and maximum counting rates for the 2.5- to 2.7-MeV window are 115 and 194 counts per 32s (high-altitude data set) and 91 and 185 counts per 32s (low-altitude data set). With the above assumptions, absolute thorium abundances are estimated from the GRS counting rate data using the following relation [*Lawrence et al.*, 1999a]:

$$C_{\mathrm{Th}} = A_{\mathrm{Th}} a t \varepsilon F_{\gamma}. \qquad (1)$$

Here, C_{Th} is the mean number of counts per 32s above background within an energy band (2.5 – 2.7 MeV) around the 2.61-MeV full energy peak, A_{Th} is the weight fraction abundance of thorium in μg/g, a is the effective GRS detector area at the lunar equator (54 cm^2 see [*Feldman et al.*, 1999]), t is the collection time for a single spectral measurement (32s), ε is the model-derived GRS detector efficiency at 2.61 MeV within the 2.5- to 2.7-MeV window (ε=0.322 counts per incident γ ray), and F_{γ} is the expected flux of thorium γ rays at the spacecraft per μg/g of thorium on the lunar surface.

Since the first estimate of LP absolute thorium abundances was published, the gamma-ray flux per μg/g of thorium [*Lawrence et al.*, 1999a, equation 2], was found to be in error. If we let $h_o = h/R_m$ where h is the spacecraft altitude (100 km) and R_m is the lunar radius (1738 km), then as described in Appendix A, F_{γ} is derived to be

$$F_{\gamma} = \frac{n_{\mathrm{Th}}\Gamma}{2\mu}\left(1 - \frac{h_o^{1/2}\left(2+h_o\right)^{1/2}}{1+h_o}\right). \qquad (2)$$

The thorium atom density is: n_{Th} = 4.02 x 10^{15} atoms/cm^3/(μg/g), the gamma-ray production rate is: Γ = 5.6 x 10^{-19} γ/s/atom, and the mean mass attenuation coefficient for 2.61 MeV γ-rays in the lunar regolith is: μ = 0.0612 cm^{-1}. With the above values, F_{γ} = 0.0124 γ s^{-1} cm^{-2} (μg/g)$^{-1}$. This is ~25% lower than the value given previously by Lawrence et al. The derived abundances presented here are therefore ~25% higher than those given by Lawrence et al.

Here we describe in detail the uncertainties of the thorium abundance measurements. Specifically, uncertainties may result from counting statistics (Poisson statistics), imperfect time-dependent corrections, and a breakdown of the assumptions given at the beginning of this section. In the following sections the uncertainties due to Poisson statistics, time-dependent corrections, and nonuniform background variations (a breakdown of assumption 1) are investigated. While we expect the uncertainties due to assumption 2 are <0.5 μg/g [*Lawrence et al.*, 1999a], a detailed knowledge of the origin of the absolute background counts is needed before this assumption can be tested.

3.1. Statistical and Data Correction Uncertainties

To estimate how much effect the time-dependent corrections (gain drifts, galactic cosmic ray variations, dead time corrections, etc.) have on the overall uncertainties, we can compare the measured variance of counts within individual spatial pixels with the uncertainties we would expect from Poisson statistics (counting time and photon statistics). Uncertainties due to Poisson statistics are the lower limit of the uncertainties that can be obtained with GRS measurements. The abundance uncertainty for a given 60 x 60 km pixel due to Poisson statistics is

$$\sigma_{\mathrm{Poisson}} = \frac{1}{a\varepsilon t F_{\gamma}}\sqrt{\frac{C_{\mathrm{Th}}}{N}}, \qquad (3)$$

where N is the number of 32s spectra measured in the pixel, $a\varepsilon t F_{\gamma}$ = 6.9 counts per μg/g is the conversion factor from equation (1), and, again, C_{Th} is the mean number of counts measured per 32s in each pixel. The measured abundance uncertainty in each pixel is

$$\sigma_{\mathrm{measured}} = \frac{1}{a\varepsilon t F_{\gamma}}\sqrt{\frac{\sum_{i=1}^{N}\left(C_{\mathrm{Th},i} - C_{\mathrm{Th}}\right)^2}{N-1}}, \qquad (4)$$

where $C_{\mathrm{Th},i}$ is the measured counts in a given 32s spectrum i. The value $\sigma_{\mathrm{measured}}$ contains uncertainties due to Poisson statistics as well as systematic uncertainties such as imperfect time-dependent corrections.

Figure 1 shows plots of the Poisson uncertainties (equation (3)) versus the measured uncertainties (equation (4)) for both uncorrected (solid circles) and corrected data (gray crosses) for the high- and low-altitude data sets. If Poisson statistics were the only source of uncertainties, then all of the data points would lie along the unity line. However, in both data sets most of the uncorrected data fall above the unity line indicating that there are significant uncertainties not due to Poisson statistics. On the other hand, much of the corrected data cluster around the unity line indicating that most of the non-Poisson uncertainties have been removed.

There are some differences between the high- and low-altitude data. The corrected high-altitude data still lie somewhat above the unity line, while the low-altitude data follow the line directly. This is not surprising, as the high-altitude data cover more time than the low-altitude data (Table 1). This longer time span for the high-altitude data both reduces the Poisson uncertainties and increases the chance of applying imperfect time-dependent corrections. In addition, there was more solar activity during the high-altitude portion of the mission than during the low-altitude portion of the mission. The increased solar activity likely increased the observed uncertainties for the high-altitude

data. Nevertheless, it is clear from Figure 1 that the time-dependent corrections are being carried out with sufficient accuracy so that uncertainties from Poisson statistics are the dominant source of measured uncertainties. Figure 2 shows the measured uncertainties from the corrected data plotted as a function of latitude in 5° wide bins. As expected for Poisson statistics, the uncertainties are the lowest at the poles and greatest near the equator.

3.2. Systematic Uncertainties Due to Background Variations

We investigate systematic uncertainties due to nonuniform background variations (i.e. the breakdown of assumption 1) using orbital, calibration, and model-derived γ-ray spectra. Figure 3 shows orbital γ-ray spectra (2 – 3 MeV) for three different 30° x 30° regions centered about the lunar equator. Region 1 (-30° < longitude < 0°) is a high-thorium region (8.5 μg/g), region 2 (15° < longitude < 45°) is a moderately high thorium region (2.5 μg/g), and region 3 (120° < longitude < 150°) is a low-thorium region (1.2 μg/g). If we invoke assumption 2 (i.e., assume that the low-thorium region has little or no thorium), then the region 3 spectrum is an approximate background spectrum for the energy window containing the thorium line.

Figure 4 shows spectra from regions 1 and 2 after the background spectrum (region 3) has been subtracted. Also shown are calibration and model-derived spectra that have been scaled to the orbital spectra. The calibration spectrum was taken with the GRS before launch and contains an uncalibrated 2.61-MeV thorium line from the naturally occurring thorium in the concrete floor and walls of the laboratory. The model spectrum was calculated using a Monte Carlo simulation of the GRS detector response [*Lawrence et al*., 1999a; *Prettyman et al*., 1998]. As seen, the correspondence is generally better for all three spectra between the energies 2.5 – 2.7 MeV than for the 2.4- to 2.8-MeV window which was used previously by *Lawrence et al*. [1998] to derive relative thorium abundances. Specifically, for the 2.4- to 2.8-MeV window, the orbital data clearly show excess counts relative to both the calibration and model spectra.

To estimate the possible magnitude of systematic uncertainties due to nonuniform background counts, a series of calculations has been carried out with the global 60 x 60 km data. The total number of counts above background have been calculated for a number of different window widths (ΔE = 0.05 – 0.4 MeV) centered about 2.61 MeV. These measured counts were normalized to the detector efficiency using the calculated model spectrum. The counts from each window width, $C_{\Delta E}$, were then compared to the counts, $C_{0.2}$, calculated using the nominal window width of 0.2 MeV. Figure 5 shows the results of these calculations where the window width is plotted versus the globally averaged ratio $<(C_{\Delta E} - C_{0.2})/C_{0.2}>$. The error bars are the calculated standard deviation of the global average. If abundance variations from the 2.61-MeV thorium line are the only source of global variations for the counts within these window widths, then the ratio $<(C_{\Delta E} - C_{0.2})/C_{0.2}>$ should be zero.

Figure 5, however, shows that as the window width increases, more counts are measured than can be accounted for by just scaling the detector efficiency. It is likely that many of the excess counts for the larger window widths result from γ-ray lines from elements other than thorium that have energies near 2.61 MeV but have fluxes and variability substantially lower than the thorium γ rays. These elements include silicon and oxygen, which likely have little variation over the Moon, as well as iron, magnesium, and aluminum, which might have larger compositional variations (see *Reedy* [1978] for a listing of γ-ray lines). In particular, we notice that the high-altitude data show a greater variability from the nominal window width than the low-altitude data. This effect may result from incomplete corrections for systematic uncertainties (see Figure 1a). In addition, the high-altitude data average over much larger areas than the low-altitude data [(150 km)^2 versus (45 km)^2]. As there are numerous regions on the Moon which are compositionally inhomogeneous over these spatial scales, these inhomogeneities may manifest themselves with greater variations in the high-altitude data.

As the window width narrows, the trend is less clear. In this case, it is possible that in addition to a nonuniform background, the peak parameters of the model spectrum used to calculate efficiencies do not exactly match the peak parameters from the orbital data. In addition, the number of counts used to make the measurement becomes quite small and Poisson variations start to become important, which may be contributing to the larger error bars. Yet in spite of these details, the variations given by Figure 5 likely represent the upper limit of nonuniform background variations that are also present in the measured abundances. Using Figure 5 as a guide, we estimate that the relative systematic errors due to nonuniform background variations are no greater than 30% (high-altitude) and 15% (low-altitude) and no less than 10% (high-altitude) and 4% (low-altitude).

3.3 Summary of Abundance Uncertainties

From the preceding discussion we conclude that systematic uncertainties from nonuniform background variations are the dominant uncertainty for most abundance measurements. For example, with the low-altitude data the abundance measurements in all pixels have an upper limit on their relative systematic uncertainties of (+4%,-15%). However, for abundances < 2 μg/g at low latitudes (see Figure 2), uncertainties due to Poisson statistics and time-dependent corrections start to be important. As the estimates of thorium abundances are improved with more detailed spectral analyses, we expect the final uncertainties to be close to the lower physical limit determined by Poisson statistics.

4. Global Thorium Abundances

4.1. High-Altitude Versus Low-Altitude Data

Thorium abundance maps for both the high- and low-altitude data are shown in Plate 1. These global maps show the derived thorium abundances overlaid with a lunar surface features map. We see the same thorium surface features that were identified in earlier studies, but now we are able to make a comparison between the two data sets. From these maps it is clear that the low-altitude data have distinctly better surface resolution than the high-altitude data. In particular, many of the high-thorium regions that appear to be contiguous in Plate 1a are resolved into distinct regions in Plate 1b. A clear example of the better resolution of the low-altitude data set is seen with the identification of the Compton/Belkovich thorium-rich region (60°N, 100°E) first reported by *Lawrence et al*. [1999a]. The size of this region is approximately 150- to 300-km in diameter, which is similar to the $(150\ \mathrm{km})^2$ surface resolution of the high-altitude data set.

The two data sets are compared directly in Figure 6, which is a plot of the derived thorium abundances for the two data sets. In Figure 6 the small points are the global data, the solid line is the unity line, and the large circles show the average low-altitude abundance within 0.5-μg/g high-altitude abundance bins. For abundances > 7 μg/g we see that the low-altitude-derived abundances are consistently higher than the high-altitude-derived abundances. If this effect is not due to systematic uncertainties (the uncertainties discussed in section 3.2 were upper limits and may be smaller), this observation suggests that the majority of regions with abundances > 7 μg/g have small areas of < $(150\ \mathrm{km})^2$ (the surface resolution of the high-altitude data). This is a reasonable interpretation because the high-altitude measurements smooth and average data over an area of $(150\ \mathrm{km})^2$. Small-area, high-thorium regions will therefore appear to have lower thorium abundances in the high-altitude measurements compared to the low-altitude measurements. It is also possible that some or all of these regions have areas which still lie unresolved in the low-altitude data set. If such regions exist, it is possible they may be identified with subsets of the low-altitude data. As seen in Table 1, 10% of the low-altitude data were taken from heights of < 20 km, so for this data subset, the surface resolution would be correspondingly better.

In contrast to the high-thorium regions, Figure 6 shows that for thorium abundances < 7 μg/g, there is a one-to-one correspondence between the two data sets. This implies that the majority of regions with thorium abundances < 7 μg/g have thorium surface distributions that appear to be homogeneous on the scale of an area > $(150\ \mathrm{km})^2$. However, as demonstrated by the Compton/Belkovich thorium anomaly (see Plate 3a and *Lawrence et al*. [1999a]), not all regions with measured thorium abundances < 7 μg/g are homogeneous on a scale of $(150\ \mathrm{km})^2$.

4.2 Thorium Abundances Versus Topography

A comparison of thorium abundances with topography is shown in Figure 7, where the topographic data of *Smith et al*. [1997] have been smoothed to the footprint of the GRS data using an equal area Gaussian smoothing algorithm. From Figure 7 it appears that the surface thorium abundances are segregated by topography into two components. For low thorium abundances, there is a general inverse correlation between topography and thorium. The lowest thorium abundances are seen at the highest elevations, while relatively higher thorium abundances are seen at the lowest elevations. This relationship was identified by *Trombka et al*. [1973] and *Metzger et al*. [1977] for the lunar equatorial regions using Apollo GRS data. With the LP data we see that this inverse relationship continues to hold for most of the lunar highlands. The existence of the low-thorium component, located mostly in the highlands and in SPA Basin (see below), suggests that the process which emplaced the thorium is global in nature. The relationship of increased thorium for lower elevations is what is expected if increasing amounts of lower crustal material are being exposed from greater depths [*Ryder and Wood*, 1977; *Ryder and Spudis*, 1987]. In particular, this thorium-topographic relationship appears to be signature of the global differentiation of the Moon [*Vaniman et al*., 1991].

In light of these data, the thorium deposition model of *Haskin* [1998] may need to be studied in greater detail. In his model, Haskin proposes that most if not all the highlands thorium was globally deposited by the Imbrium impact. While there is evidence for such deposition [see *Lawrence et al*., 1998, Figure 5], the Haskin model needs to be understood within the context of the topographic-highlands thorium relationship seen in Figure 7.

In contrast to the inverse topography-thorium relationship seen in the highlands, the high-thorium regions which exist on the nearside show very little if any correlation with topography. This observation suggests that the nearside thorium was emplaced by a fundamentally different process than most of the farside highlands thorium. However, one location that might show a slight positive correlation with topography is the region surrounding Fra Mauro, which contains some of the largest observed thorium abundances seen on the Moon (open circles and inset). The Fra Mauro data of Figure 7 were selected to show all of the pixels within the region of (15°S – 20°N, 45°W – 0°) having thorium abundances > 6 μg/g. This selection defines a high-thorium region which roughly extends from the Carpathian Mountains at (15°N, 30°W) to Lalande crater at (4°S, 9°W). The inset shows the mean topography (solid circles) and 25th and 75th percentiles (lines) for 0.75-μg/g thorium abundance bins.

The thorium-topography relationship around Fra Mauro is important because there has been controversy regarding the nature of the high-thorium material in the Fra Mauro region. Some investigators suggest that most of the material within the Fra Mauro region consists of

primary Imbrium ejecta [*Wilhelms*, 1987, and references therein], while others maintain that most of the material within Fra Mauro is derived from secondary ejecta and/or KREEP volcanism [*Hawke and Head*, 1978, and references therein]. The slight positive topography-thorium correlation seen with the LP data is not consistent with the analysis of *Hawke and Head* [1978], where an inverse topography/thorium relation was identified for areas around Fra Mauro using Apollo GRS data. Specifically, Hawke and Head showed that for a region extending from Ptolemaeus to Fra Mauro to Mare Cognitum, the thorium abundances increased for lower depths. This observation was interpreted as evidence that the high-thorium material in Fra Mauro was possibly deposited by KREEP volcanism. However, with the new LP data, it seems more appropriate to study the topographic-thorium relationship in the Fra Mauro region using the high-thorium boundary that is clearly defined by the data (as described above). This high-thorium boundary likely represents a more distinct terrain than the highland-mare boundary studied by Hawke and Head. With the newly defined boundary, the inverse relation of Hawke and Head is certainly no longer seen and there may even be a slight positive correlation. Detailed studies using additional information such as the geologic maps of *Wilhelms* [1987] and remotely sensed iron and titanium abundance data from Clementine and Lunar Prospector will certainly provide more understanding of the nature of the topography-thorium relationship in the Fra Mauro region.

5. Regional Thorium Abundances

In this section we investigate a number of regions using the low-altitude thorium data. Some of these regions have been places of interest for a long time (SPA Basin, Tycho crater), and others have been identified as thorium anomalies for the first time using the LP data (Compton/Belkovich, western Tranquillitatis).

5.1. South Pole-Aitken Basin

SPA Basin is the largest impact basin on the Moon with a depth of 12 km and diameter of 2500 km [*Spudis et al*., 1994]. Because of its great size, the impact which created this basin excavated material deep from the lunar crust and maybe even from the mantle. In fact, recent studies using data from Clementine have shown that SPA Basin is a distinct region containing compositions thought to be derived from either the lower crust [*Pieters et al*., 1997] or a combination of mantle and lower crustal material [*Lucey et al*., 1998]. Other studies of LP data have also shown that SPA Basin is compositionally distinct [*Lawrence et al*., 1998, 1999a; *Feldman et al*., 1998; *Elphic et al*., 1998, this issue].

Plate 2 shows three different views of SPA basin. Plate 2a shows the low-altitude thorium abundances, Plate 2b shows FeO abundances derived from CSR data by *Lucey et al*. [this issue], and Plate 2c shows topography data given by *Smith et al*. [1997]. The thorium within SPA appears to segregate into two components: a low-abundance, diffuse component and a moderately high abundance, localized component.

The low-abundance thorium component has an average concentration of 2 – 4 μg/g and is distributed over the entire basin, as delineated by both FeO and topography data. With some exceptions the low-abundance component appears to follow the general trend with topography that is seen for the highlands thorium abundances (see Figure 7). Specifically, the deepest part of SPA is in the southern portion, and this is also where the highest thorium abundances of the low-abundance component are located. One notable exception to this trend is found at Apollo basin (36°S, 152°W). Portions of Apollo basin extend to more than 5 km below the mean lunar radius, and the thorium abundances in this region are distinctively low compared to the surrounding regions. However, as seen in the FeO data and in the geologic maps of *Wilhelms* [1987], these locations within Apollo are filled with high-FeO mare basalt. Another location which does not appear to follow the highlands topography-thorium relationship is at the three craters Minnaert (68°S, 180°), Antoniadi (70°S, 172°W), and Numerov (71°S, 161°W). While all three craters show up in Plate 2c as topographic lows, the middle crater, Antoniadi, appears to show relatively less thorium than its two neighbors. According to Wilhelms, Antoniadi is the only crater of this trio which also has mare basalt fill. Other locations having high-FeO mare basalts while also containing relatively low thorium abundances include Leibnitz (38°S, 179°E), Poincare (57°S, 164°E), and Mare Ingenii (34°S, 164°E). This observation that mare basalts within SPA Basin may contain relatively low thorium abundances is contrary to what was described by *Hawke and Spudis* [1980] using Apollo GRS data. However, since the uncertainties of these low-abundance data may be large, this mare basalt-thorium relation needs to be confirmed with more detailed regional studies and data analysis.

In contrast to the large-area, low-abundance component, the moderately high-abundance thorium component is concentrated in the northwest portion of SPA Basin with two abundance maxima centered near Birkeland crater (30°S, 173°E) and an unnamed crater (41°S, 165°E) between the craters Obruchev (39°S, 162°E) and Oresme (42°S, 169°E). However, it does not appear that the high-thorium component is directly associated with these craters. The entire high-thorium component extends roughly from (22°S, 180°) to (50°S, 160°E). One reason we consider this region to be a different thorium component is that it does not follow the highlands topographic-thorium relationship of Figure 7. In fact, the highest elevations inside SPA are at the same place where we see this high-abundance component. We also note that the outlines of this component do not appear to be correlated with the optically derived FeO and TiO_2 [*Lucey et al*., this issue] (not shown) abundances.

When the above observations are connected with the topography-thorium relationship of Figure 7, we conclude that the low abundance component seen in SPA Basin is likely part of the global highlands thorium component in which higher-thorium, lower crustal material is being exposed. This interpretation is consistent with the *Lucey et al*. [1998] explanation that much of the material within SPA basin has a one-to-one composition of mantle and lower crustal material.

In contrast, the high-abundance component does not follow the highlands topographic-thorium relationship and does not appear to be correlated with the optically estimated FeO and TiO_2 abundances. We therefore suggest that the high-abundance component was emplaced by a process that is fundamentally different than the process which emplaced the low-abundance component. One possible explanation for the existence of the high-abundance component is that it is associated with ancient mare basalt deposits that were covered over as a result of extensive mass wasting caused by seismic waves from the Imbrium impact event [*Hawke and Spudis*, 1980]. However, as was described earlier, we see indications of an anti-correlation of thorium with exposed mare basalt, not a correlation. If the ancient mare basalt units described by Hawke and Spudis are similar to the exposed mare basalts, then ancient mare basalts would not be the source of the high thorium abundances. There are other reasons such a scenario appears unlikely. The layer covering the ancient mare deposits would have to be very thin (~30 g/cm^2 [see *Evans et al*., [1993]) so that the thorium γ rays could penetrate the layer. Since 10 – 100 cm of lunar soil is reworked every 10^9 years [*McKay et al*., 1991; *Langevin and Arnold*, 1977], a covering of <30 g/cm^2 would probably not survive the 3 – 4 x 10^9 years since the Imbrium impact. Another explanation for the high-thorium region could be the existence of a very high density of high-thorium, dark halo craters over very large areas (the southern portion of the high-abundance component has an area of roughly 240 x 360 km). However, it is unlikely that there exists a density of dark halo craters large enough to create the large thorium signal we see over such large areas. For example, *Blewett et al*. [1999] identified an unnamed dark halo crater (39°S, 157°E) as having high FeO and TiO_2 abundances. This crater, however, is not located within the region containing the highest thorium abundances. If other dark halo craters behave similarly, it is therefore unlikely that covered over basalt deposits are the source of the high-thorium regions.

Another possible explanation for the existence of the high-thorium component is that because it is located very close to the antipode of Imbrium basin, it might be ejecta from the Imbrium impact, as suggested by *Haskin* [1998] and *Haskin et al*. [1998]. While intriguing, these data need to be investigated in more detail and compared with other data sets before such a conclusion is shown to be compelling.

5.2 Compton/Belkovich Thorium Anomaly in the Northern Highlands

Most of the lunar highland regions have low thorium abundances of < 2 μg/g. However, one location of anomalously high thorium abundances is the Compton/Belkovich region in the northeastern highlands [*Lawrence et al*., 1999a]. This anomalous high-thorium region (Plate 3a) is located at (60°N, 100°E) between the craters Compton (55°N, 105°E) and Belkovich (63°N, 90°E). The measured thorium abundances range from 3 to 6 μg/g over an area of 150 – 300 km^2. While not shown, an investigation of raw γ-ray spectra shows that this region also has anomalously high potassium abundances. The potassium abundance, however, cannot be quantified until the full spectral deconvolution analysis is carried out with the GRS data. Because the GRS measures thorium abundances averaged over large areas, it is not clear from these data whether this high-thorium anomaly has a small size of <(45 km)^2 with high thorium abundance (> 6 μg/g) or if it is ~(150 km)^2 in size with a moderately high thorium abundance (3 – 6 μg/g). The optically derived FeO abundances in this region (Plate 3b) [*Lucey et al*., this issue] show no anomalous features for the location of the high-thorium anomaly. The FeO abundances look very much like normal highlands material with values in the broad range of 0 – 6 wt%. TiO_2 measurements from Clementine (not shown) also indicate very low abundances. In a complementary analysis carried out by *Thomsen et al*. [1999], it is further found that no other location on the Moon has such high thorium abundances coincident with such low FeO and TiO_2 abundances; that is, this location is compositionally unique on the Moon. Finally, the topography in this region (Plate 3c) [*Smith et al*., 1997] shows a relative depression almost coincident with the location of the high-thorium anomaly. We currently do not understand how this topographic depression relates to the thorium anomaly.

From the composition data it appears that we are identifying a concentration of highly evolved material in the Compton/Belkovich region. Specifically, the high thorium and low iron and titanium abundances suggest that this region may contain high concentrations of alkali anorthosite and/or granite. *Korotev* [1998] has compiled elemental abundances (Al, Ti, Fe, K, Th, and U) for a number of different types of highly evolved igneous rocks. *Taylor et al*. [1991, and references therein] also list measured bulk compositions for evolved lunar samples. The average thorium abundance for 10 different granites and/or felsites is 36±13 μg/g [*Korotev*, 1998]. In contrast, the average thorium abundance for alkali anorthosites is 4.8±3.3 μg/g. If the Compton/Belkovich anomaly is indeed dominated by granite, then it must be a small area with very high thorium abundances. We can test for the presence of granite by looking at potassium, silicon, and possibly iron abundances. The potassium to thorium ratio for granite should be over 50% greater (970 versus 416 [see *Korotev*, 1998,

Figure 1]) than would be expected for a rock having KREEP-type ratios. As previously mentioned, we do see an anomalously high potassium abundance in the raw count rate data, but the raw potassium counts do not deviate significantly from the constant potassium to thorium count rate ratio that is seen over the whole Moon [*Lawrence et al*., 1998]. However, since the potassium abundance has not been quantified with the spectral deconvolution analysis, we cannot conclusively determine if the potassium abundance is larger than would be expected for normal KREEP ratios. Regarding silicon abundances, *Taylor et al*. [1991] and *Haskin and Warren* [1991] show that SiO_2 abundances should be over 30% larger for granite compared to most other lunar rock types (73 wt% versus 40 – 50 wt%). While the strongest silicon γ-ray line at 1.78 MeV should be sensitive to such an abundance difference, a determination of the relative silicon abundance has not yet been carried out because there are a number of thorium and uranium lines that interfere with the silicon line. Finally, iron abundance measurements might help to discriminate what type of material dominates the anomalous thorium region. According to *Korotev* [1998], the average FeO abundance of granite and felsite is 7.7±3.9 wt%, and the average alkali anorthosite abundance is 2.8±1.0 wt%. A close inspection of the 0.25° x 0.25° FeO map by *Lucey et al*. [this issue] shows a noisy salt and pepper distribution with FeO abundances generally ranging from 4 – 5 wt% in the eastern part of the anomaly to 1 – 2 wt% in the western part of the anomaly. If the Clementine-derived FeO abundances represent the true iron abundances and the potassium abundances are present in KREEP-like ratios as suggested by the initial analysis, then both these datasets suggest that the dominant lithology in this region is more like an alkali anorthosite than a granite.

5.3 Other Regions of Interest

We have identified an isolated high thorium concentration within the western portion of Mare Tranquillitatis. Plate 4 shows a map of thorium abundances for the western Tranquillitatis region. As seen, the high thorium concentration is centered on the crater Arago, a 26-km-diameter crater located at (6.2°N, 21.4°E). The measured thorium abundance around Arago is between 5 and 7 μg/g and shows an asymmetric thorium distribution where the higher thorium abundances are located to the west of Arago. We also note that highland material excavated from beneath the mare by Arago was mapped using Clementine data by *Staid et al*. [1996]. Staid et al. showed that the larger crater Plinius (15.4°N, 23.7°E) also excavated highland material from beneath the mare, but Plate 4 shows that it does not exhibit a high-thorium anomaly. The existence of this high-thorium anomaly at Arago crater is therefore interesting because it shows that there were at least some high-thorium regions not directly located beneath the Imbrium/Procellarum region and is evidence for some degree of thorium inhomogeneity at depth on the lunar nearside.

The last region we describe here is Tycho crater (43°S, 11°W). In contrast to the high thorium abundances seen elsewhere, Tycho shows some of the lowest thorium abundances seen on the entire Moon. Plate 5 shows a map of thorium abundances and Clementine albedo data [*Robinson et al.*, 1999] in the region around Tycho. Plate 5a shows that the area around Tycho has very low thorium abundances, with the lowest abundances located directly over Tycho. We also note that low thorium abundances appear to overlie much of the Tycho's ray structure, particularly the ray structure northeast of Tycho.

As explained by *Pieters* [1986, 1993], the areas in and around Tycho appear to be enriched by a gabbroic high-calcium pyroxene which is thought to be plutonic in nature. In regards to KREEP abundances of plutonic rocks, *Korotev* [1998] predicted that while some rocks from the Apollo 15 and 17 collections such as norite and troctolite (and by extension gabbro) may have assimilated a KREEP component during their formation, such plutonic rocks that occur away from Imbrium basin (where the large KREEP abundances are found) may have substantially lower concentrations of radioactive elements. This is indeed what is seen with the thorium data at Tycho. If the gabbroic material identified by Pieters represents an excavated plutonic structure, then this material did not assimilate KREEP which suggests that KREEP was absent at depth from at least this portion of the Moon.

6. Summary

In this paper, we have presented an overview of the lunar thorium abundances and uncertainties that have been measured using the Lunar Prospector Gamma-Ray Spectrometer. Specifically, we have shown that the measured uncertainties for both the high- and low-altitude data are < 0.5 μg/g. Other systematic uncertainties may be somewhat larger, but with future analysis, we expect to be able to reduce significantly the uncertainties from variations in background counts.

Comparisons of the high- and low-altitude thorium abundance data show a very good correspondence, especially for thorium abundances < 7 μg/g. Because of the smaller spatial resolution of the low-altitude data, we see evidence that a significant portion of the regions with thorium abundances > 7 μg/g may likely be small-area regions ≤ $(150\ km)^2$. From the low-altitude data we see that some of these small-area, high-thorium regions are directly related to craters on the nearside. While most of these craters are located around the rim of Imbrium basin [*Lawrence et al*., 1999a], we have identified at least one high-thorium crater (Arago) in western Tranquillitatis not directly associated with Imbrium basin.

As delineated by topography, it appears that thorium has been globally emplaced by at least two different processes. For the highlands regions and much of SPA Basin

the low to moderate thorium abundance is inversely correlated with topography. This is the signature one expects if the Moon underwent a global differentiation process with more mafic and thorium rich materials increasing in abundance at lower depths. While there is evidence to show that thorium in the highlands may have been globally emplaced by the Imbrium impact [*Haskin*, 1998; *Lawrence et al*., 1998], this interpretation needs to be reconciled with the topographic-thorium relationship we observe here.

Exceptions to the global topographic-thorium distribution have been identified in a number of locations. The highest-thorium region in SPA is located not in a topographic low, but at the highest elevations within SPA. This suggests that the thorium in this location was emplaced by a process different from the one which emplaced much of the thorium elsewhere in SPA and the highlands. The Compton/Belkovich high-thorium anomaly, while located in a topographic low point, shows no mafic anomalies. This suggests that this region may be enriched with evolved lithologies, and to date it represents the only such extended region on the Moon that has been identified. Finally, the low thorium abundances at Tycho crater, which is thought to be an excavated plutonic complex, demonstrate that thorium (and by extension KREEP) was not assimilated at depth in this portion of the Moon.

Appendix A: Derivation of $F\gamma$

The γ-ray flux per μg/g of thorium (equation 2) can be derived by assuming spherical geometry for the LP spacecraft orbiting the Moon. Figure A1 shows the geometry where R_m is the lunar radius, h is the spacecraft height above the lunar surface, r is the distance from the spacecraft to a differential volume element dV, R is the distance from the Moon's center to dV, x is the distance from dV to the lunar surface, and d is the distance a γ-ray travels through the lunar regolith to reach the spacecraft. The angles α, δ, and θ are defined as shown in Figure A1. From Figure A1, the differential volume element dV can be expressed as

$$dV = R\sin\delta d\varphi \;\; Rd\delta \;\; dR \qquad \text{(A1)}$$

where φ is the longitude angle. Since the γ-rays only come from the top few meters of the lunar regolith, $R \sim R_m$ and dV can be approximated by (where dR is now dx)

$$dV = R_m^2 d(\cos\delta)dxd\varphi\ . \qquad \text{(A2)}$$

The number of γ-rays produced in this volume element is $n_{\mathrm{Th}}\Gamma dV$ where n_{Th} is the thorium atom density (assumed to be constant with depth) and Γ is the γ-ray production rate per μg/g of thorium (see section 3).

The differential flux on an isotropic detector a distance r away is then

$$dF = \frac{n\Gamma R_m^2 e^{-\mu d}}{4\pi r^2} d(\cos\delta)dxd\varphi \qquad \text{(A3)}$$

where the exponential term accounts for the attenuation of γ-rays having a mass attenuation coefficient μ going through a distance $d=x/\cos\alpha$ of lunar regolith (see the inset of Figure A1). The total flux is found by integrating equation A3 over the whole Moon:

$$F = \frac{n\Gamma R_m^2}{4\pi} \int_{\cos\delta}\int_{x}\int_{\varphi} \frac{e^{-\mu x/\cos\alpha(\delta)}}{r(\delta)^2} d(\cos\delta)dxd\varphi \qquad \text{(A4)}$$

where r and $\cos\alpha$ are both functions of the angle δ. The limits of integration are $\varphi = 0$ to 2π, $x = 0$ to ∞, and $\cos\delta = 1$ to $R_m/(R_m+h)$. The φ and x integrals are carried out in a straightforward manner to give

$$F = \frac{n\Gamma R_m^2}{2\mu} \int_{\cos\delta=1}^{R_m/(R_m+h)} \frac{\cos\alpha(\delta)}{r(\delta)^2} d(\cos\delta)\ . \qquad \text{(A5)}$$

Now, using the following geometric relations

$$\begin{aligned} (R_m + h)\sin\theta &= R\sin\alpha \\ &\approx R_m \sin\alpha \\ R_m \sin\delta &= r\sin\theta \\ R_m + h &= R_m\cos\delta + r\cos\theta \end{aligned} \qquad \text{(A6)}$$

$\cos\alpha$ and r can be expressed in terms of δ (where $\beta = 1 + h/R_m$)

$$\begin{aligned} \cos\alpha(\delta) &= -\frac{\beta\cos\delta - 1}{\left(\beta^2 - 2\beta\cos\delta + 1\right)^{1/2}} \\ r(\delta)^2 &= R_m^2\left(\beta^2 - 2\beta\cos\delta + 1\right) \end{aligned} \quad . \qquad \text{(A7)}$$

Equation A5 now becomes

$$F = -\frac{n\Gamma}{2\mu} \int_{\cos\delta=1}^{R_m/(R_m+h)} \frac{\beta\cos\delta - 1}{\left(\beta^2 - 2\beta\cos\delta + 1\right)^{3/2}} d(\cos\delta)\ . \qquad \text{(A8)}$$

Equation A8 can be analytically integrated to obtain equation 2.

Acknowledgments. The authors would like to thank Carlé Pieters and Larry Haskin for their helpful reviews. The authors would also like to thank Mark Wieczorek for pointing out the problem with the original gamma-ray flux derivation and informing us in time to include the new derivation in this paper. Finally, David Lawrence thanks the JGR editorial staff for their patience in waiting for this paper as the community of Los Alamos was busy recovering from the recent wildfire. This work was supported by NASA through the Lunar Data Analysis Program and conducted under the auspices of the U.S. Department of Energy.

References

Blewett, D. T., G. J. Taylor, P. G. Lucey, B. R. Hawke, and J. Gillis, High-resolution, quantitative remote sensing of South Pole-Aitken Basin, *Lunar Planet. Sci. Conf. 30th*, abstract 1438, 1999.

Elphic, R. C., S. Maurice, D. J. Lawrence, W. C. Feldman, B. L. Barraclough, A. B. Binder, and P. G. Lucey, Lunar Fe and Ti abundances: Comparison of Lunar Prospector and Clementine data, *Science*, *281*, 1493, 1998.

Elphic, R. C., D. J. Lawrence, W. C. Feldman, B. L. Barraclough, S. Maurice, A. B. Binder, and P. G. Lucey, Lunar rare earth distribution and ramifications for FeO and TiO_2: Lunar Prospector neutron spectrometer observations, *J. Geophys. Res*., this issue.

Evans, L. G., R. C. Reedy, and J. I. Trombka, Introduction to planetary remote sensing gamma ray spectroscopy, in *Remote Geochemical Analysis: Elemental and Mineralogical Composition*, edited by C. M. Pieters and P. A. J. Englert, p.167–198, Cambridge Univ. Press, New York, 1993.

Feldman, W. C., B. L. Barraclough, S. Maurice, R. C. Elphic, D. J. Lawrence, D. R. Thomsen, and A. B. Binder, Major compositional units of the Moon: Lunar Prospector thermal and fast neutrons, *Science*, 281, 1489, 1998.

Feldman, W. C., B. L. Barraclough, K. R. Fuller, D. J. Lawrence, S. Maurice, M. C. Miller, T. H. Prettyman, and A. B. Binder, The Lunar Prospector gamma-ray and neutron spectrometers, *Nucl. Instrum. and Methods Phys. Res., Sec. A*, 422, 562, 1999.

Haskin, L. A., The Imbrium impact event and the thorium distribution at the lunar highlands surface, *J. Geophys. Res*., *103*, 1679, 1998.

Haskin, L. A., and P. Warren, Lunar chemistry, in *Lunar Sourcebook*, edited by G. H. Heiken, D. T. Vaniman, and B. M. French, p.357–474, Cambridge Univ. Press, New York, 1991.

Haskin, L. A., R. L. Korotev, K. M. Rockow, and B. L. Jolliff, The case for an Imbrium origin of the Apollo thorium-rich impact-melt breccias, *Meteorit. Planet Sci*., *33*, 959, 1998.

Hawke, B. R., and J. W. Head, Lunar KREEP volcanism: Geologic evidence for history and mode of emplacement, *Proc. Lunar Planet. Sci. Conf. 9th*, 3285, 1978.

Hawke, B. R., and P. D. Spudis, Geochemical anomalies on the eastern limb and farside of the Moon, in *Proceedings of the Conference on the Lunar Highlands Crust*, edited by J. J. Papike and R. B. Merrill, p.467, Pergamon, New York, 1980.

Korotev, R. L., Concentrations of radioactive elements in lunar materials, *J. Geophys. Res*., *103*, 1691, 1998.

Korotev, R. L., A new estimate of the composition of the feldspathic upper crust of the Moon, *Lunar Planet. Sci. Conf. 30th*, abstract 1303, 1999.

Langevin, Y., and J. R. Arnold, The evolution of the lunar regolith, *Annu. Rev. Earth Planet. Sci., Vol. 5*, 449, 1977.

Lawrence, D. J., W. C. Feldman, B. L. Barraclough, A. B. Binder, R. C. Elphic, S. Maurice, and D. R. Thomsen, Global elemental maps of the Moon: The Lunar Prospector Gamma-Ray Spectrometer, *Science*, *284*, 1484, 1998.

Lawrence, D. J., W. C. Feldman, B. L. Barraclough, R. C. Elphic, S. Maurice, A. B. Binder, M. C. Miller, and T. H. Prettyman, High resolution measurements of absolute thorium abundances on the lunar surface, *Geophys. Res. Lett*., *26* (17), 2681, 1999a.

Lawrence, D. J., S. Maurice, and W. C. Feldman, Software Interface Specification (SIS) for the Lunar Prospector Spectrometer Planetary Data System Files, Version V001 and Version V002, NASA Planetary Data System, Geosciences Node, Washington University, St. Louis and *Los Alamos Nat. Lab. Rep. LAUR-99-2753 and LAUR-99-2754*, Los Alamos, N.M., 1999b.

Lucey, P. G., G. J. Taylor, B. R. Hawke, and P. D. Spudis, FeO and TiO_2 concentrations in the South Pole-Aitken basin: Implications for mantle composition and basin formation, *J. Geophys. Res*., *103*, 3701, 1998.

Lucey, P. G., et al., Lunar iron and titanium abundance algorithms based on final processing of Clementine UVVIS images, *J. Geophys. Res*., this issue.

McKay, D. S., G. Heiken, A. Basu, G. Blanford, S. Simon, R. Reedy, B. M. French, and J. Papike, The lunar regolith, in *Lunar Sourcebook*, edited by G. H. Heiken, D. T. Vaniman, and B. M French, p. 285–356, Cambridge Univ. Press, New York, 1991.

Metzger, A. E., E. L. Haines, R. E. Parker, and R. G. Radocinski, Thorium concentrations in the lunar surface, I, Regional values and crustal content, *Proc. Lunar Sci. Conf. 8th*, 949, 1977.

Pieters, C. M., Composition of the lunar highland crust from near-infrared spectroscopy, *Rev. Geophys.*, *24* (3), 557, 1986.

Pieters, C. M., Compositional diversity and stratigraphy of the lunar crust derived from reflectance spectroscopy, in *Remote Geochemical Analysis: Elemental and Mineralogical Composition*, edited by C. M. Pieters and P. A. J. Englert, p.309–339, Cambridge Univ. Press, New York, 1993.

Pieters, C. M., S. Tomkins, J. W. Head, and P. C. Hess, Mineralogy of the mafic anomaly in the South Pole-Aitken Basin: Implications for excavation of the lunar mantle, *Geophys. Res. Lett*., *24*, 1903, 1997.

Prettyman, T. H., C. S. Cooper, P. N. Luke, P. A. Russo, M. Amman, and D. J. Mercer, Physics-based generation of gamma-ray response functions for CdZnTe detectors, *J. Radioanal. Nucl. Chem*., *233*, 257, 1998.

Reedy, R. C., Planetary gamma-ray spectroscopy, *Proc. Lunar Planet. Sci. Conf. 9th*, 2961, 1978.

Reedy, R. C., J. R. Arnold, and J. I. Trombka, Expected γ-ray emission spectra from the lunar surface as a function of chemical composition, *J. Geophys. Res*., *78*, 5847, 1973.

Robinson, M. S., A. S. McEwen, E. Eliason, E. M. Lee, E. Malaret, and P. G. Lucey, Clementine UVVIS global mosaic: A new tool for understanding the lunar crust, *Lunar Planet. Sci. Conf. 30th*, abstract 1931, 1999.

Ryder, G., and P. Spudis, Chemical composition and origin of Apollo 15 impact melts, *J. Geophys. Res*., *92* (B4), E432, 1987.

Ryder, G. and J. A. Wood, Serenitatis and Imbrium impact melts: Implications for large-scale layering in the lunar crust, *Proc. Lunar Sci. Conf. 8th*, 655, 1977.

Smith, D. E., M. T. Zuber, G. A. Neumann, and F. G. Lemoine, Topography of the Moon from the Clementine LIDAR, *J. Geophys. Res*., *102*, 1591, 1997.

Spudis, P. D., R. A. Reisse, and J. J. Gillis, Ancient multiring basins on the Moon revealed by Clementine laser altimetry, *Science*, *266*, 1848, 1994.

Staid, M. S., C. M. Pieters, and J. W. Head III, Mare Tranquillitatis: Basalt emplacement history and relation to lunar samples, *J. Geophys. Res*., *101* (E10), 23213, 1996.

Taylor, G. J., P. Warren, G. Ryder, J. Delano, C. Pieters, and G. Lofgren, Lunar rocks, in *Lunar Sourcebook*, edited by G. H. Heiken, D. T. Vaniman, and B. M. French, p.183–284, Cambridge Univ. Press, New York, 1991.

Thomsen, D. R., D. J. Lawrence, D. Vaniman, W. C. Feldman, B. L. Barraclough, S. Maurice, P. G. Lucey, and A. B. Binder, Global geochemical variation on the lunar surface: A three element approach (abstract), *New Views of the Moon II: Understanding the Moon through the Integration of Diverse Datasets*, Lunar and Planet. Inst., Houston, Tex., 1999.

Trombka, J. I., J. R. Arnold, R. C. Reedy, L. E. Peterson, and A. E. Metzger, Some correlations between measurements by the Apollo gamma-ray spectrometer and other lunar correlations, *Proc. Lunar Sci. Conf. 4th*, 2847, 1973.

Vaniman, D., J. Dietrich, G. J. Taylor, and G. Heiken, Exploration, samples, and recent concept of the Moon, in *Lunar Sourcebook*, edited by G. H. Heiken, D. T. Vaniman, and B. M. French, p.5–26, Cambridge Univ. Press, New York, 1991.

Warren, P. H., The magma ocean concept and lunar evolution, *Annu. Rev. Earth Planet. Sci.*, *13*, 201, 1985.
Warren, P. H., and J. T. Wasson, The origin of KREEP, *Rev. Geophys.*, *17*, 73, 1979.
Wilhelms, D. E., The geologic history of the Moon, *U.S. Geol. Surv. Prof. Pap.*, *1348*, 302, 1348, 1987.

B. L. Barraclough, R. C. Elphic, W. C. Feldman, and D. J. Lawrence, Los Alamos National Laboratory, Group NIS-1, Mail Stop D466, Los Alamos, NM 87545. (djlawrence@lanl.gov)
A. B. Binder, Lunar Research Institute, Tucson, AZ 85747.
S. Maurice, Observatoire Midi-Pyrénées, 14 Avenue Edouard Belin, 31400 Toulouse, France.
M. C. Miller, Lawrence Livermore National Laboratory, Livermore, CA 94551.
T. H. Prettyman, Los Alamos National Laboratory, Group NIS-5, Los Alamos, NM 87545.

(Received September 8, 1999; revised March 13, 2000; accepted March 24, 2000.)

[1]Los Alamos National Laboratory, Los Alamos, New Mexico.
[2]Lunar Research Institute, Tucson, Arizona.
[3]Observatoire Midi-Pyrénées, Toulouse, France.
[4]Lawrence Livermore National Laboratory, Livermore, California.

Copyright 2000 by the American Geophysical Union.

Paper number 1999JE001177.
0148-0227/00/1999JE001177$09.00

Figure 1. Plot of Poisson uncertainties versus measured uncertainties for (a) high-altitude and (b) low-altitude data. The solid circles show the data before time-dependent corrections (i.e., corrections for gain variations, cosmic ray variations, etc.) have been made. The gray crosses show the data after these corrections have been made. The solid line is the unity line for which Poisson uncertainties equal the measured uncertainties.

Figure 2. Measured uncertainties for the corrected (a) high-altitude and (b) low-altitude data versus latitude. The solid heavy line shows the mean uncertainty for 5° wide latitude bins, and the vertical lines show the 25th and 75th percentile values for the 5° wide latitude bins.

Figure 3. Orbital γ-ray spectra of three different 30° x 30° regions on the Moon from the (a) high-altitude and (b) low-altitude data. Region 1 (15°S – 15°N, 30°W – 0°) has high thorium concentrations (8.5 μg/g), region 2 (15°S – 15°N, 15°E – 45°E) has medium high thorium concentrations (2.5 μg/g), and region 3 (15°S – 15°N, 120°E – 150°E) has low thorium concentrations (1.2 μg/g).

Figure 4. Background subtracted γ-ray spectra for regions 1 and 2. High-altitude data are shown in Figures 4a and 4b, and low-altitude data are shown in Figures 4c and 4d. Also shown are the laboratory calibration and model-derived spectra which have been scaled to the measured orbital spectra. The 2.6-MeV thorium peak is clearly seen in all spectra. The peak at 2.1 MeV in the model spectrum is the first escape peak from the 2.6-MeV thorium line. In the laboratory and orbital spectra this peak appears shifted because there likely is a 2.2-MeV line from uranium in the laboratory data and 2.2-MeV lines from uranium and aluminum in the orbital data superimposed on the 2.1-MeV thorium escape peak.

Figure 5. Global average of the value $(C_{\Delta E} - C_{0.2})/C_{0.2}$ versus the selected window width around the 2.61-MeV γ-ray line for high-altitude data (open squares) and low-altitude data (solid circles). The error bars are the measured standard deviations of the global average. The vertical line is the full-width, half maximum of the model and calibration peak (0.187 MeV).

Plate 1. Global maps of measured thorium abundances for (a) high-altitude data and (b) low-altitude data.

Figure 6. Plot of measured thorium abundances for high- and low-altitude data (Figure 6a). The small circles show the measured abundances for each 2° x 2° pixel, the solid line is the unity line, and the large solid circles show the average low-altitude abundance value for 0.5-μg/g-wide bins of high-altitude abundances. Figure 6b shows the residual low-altitude abundance that lies either above or below the unity line for each of the 0.5-μg/g high-altitude abundance bins.

Figure 7. Measured thorium abundances versus topography measurements smoothed to the footprint of the (a) high-altitude and (b) low-altitude data. The inset in each plot shows the mean topography (solid circles) and 25th and 75th percentile values (vertical lines) within 0.75-μg/g-wide thorium abundance bins for the Fra Mauro region, as described in the text.

Plate 2. South Pole-Aitken Basin as seen with three different data sets (color coded) overlaid with a lunar surface features map. Plate 2a shows thorium abundances from the low-altitude data set, Plate 2b shows optically derived FeO abundances from *Lucey et al*., [this issue], and Plate 2c shows topographic data taken from *Smith et al*. [1997]. The brown color indicates that the data are either offscale or not available.

Plate 3. North pole region as seen with three different data sets (color coded) overlaid with a lunar surface features map. Plate 3a shows thorium abundances from the low-altitude data set, Plate 3b shows optically derived FeO abundances from *Lucey et al*. [this issue], and Plate 3c shows topographic data taken from *Smith et al*. [1997]. The Compton/Belkovich thorium anomaly is located at (60°N, 100°E). The brown color indicates that the data are either offscale or not available.

Plate 4. Thorium abundances overlaid with a lunar surface features map seen for the western Tranquillitatis region. The brown color indicates that the data are either offscale or not available.

Plate 5. Tycho crater as seen with two different data sets (color coded) overlaid with a lunar surface features map. Plate 5a shows thorium abundances from the low-altitude data set, and Plate 5b shows albedo data taken from *Robinson et al*. [1999].

Figure A1. Spherical geometry for a spacecraft orbiting a distance h away from the Moon having a radius R_m.

Table 1. Mean Height and Number of Spectra Collected for the High- and Low-altitude Data Sets

	High-Altitude Data Set	Low-Altitude Data Set
Dates	Jan. 16, 1998 to Dec. 19, 1998	Dec. 19, 1998 to July 31, 1999
Type	high-altitude, spin axis north and south	low-altitude, spin axis south
Mean height, km	99.8	32.3
Tenth and ninetieth height percentiles	88.5/111.2	20.9/43.8
Number of 32-s spectra	787,096	517,378
Spectra per 60x60 km pixel for $\lambda = \pm 90°, \pm 45°, 0°$	2500, 62, 50	1600, 41, 34
Percentage of possible spectra	86.3	86.9

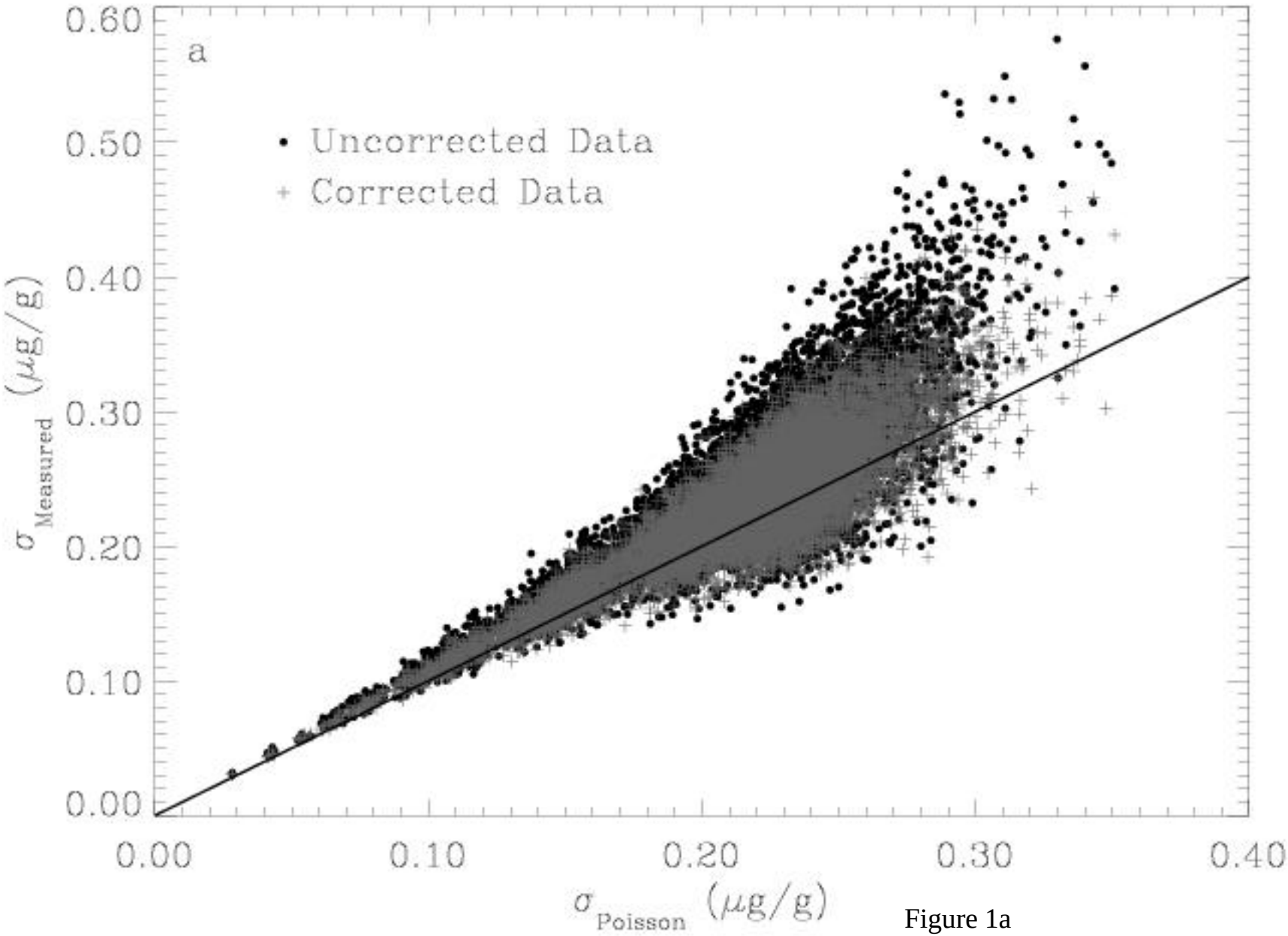
a
Uncorrected Data
Corrected Data
0.60
0.50
0.40
0.30
0.20
0.10
0.00
0.00
0.10
0.20
0.30
0.40
σ_{Measured} $(\mu g/g)$
σ_{Poisson} $(\mu g/g)$

Figure 1a

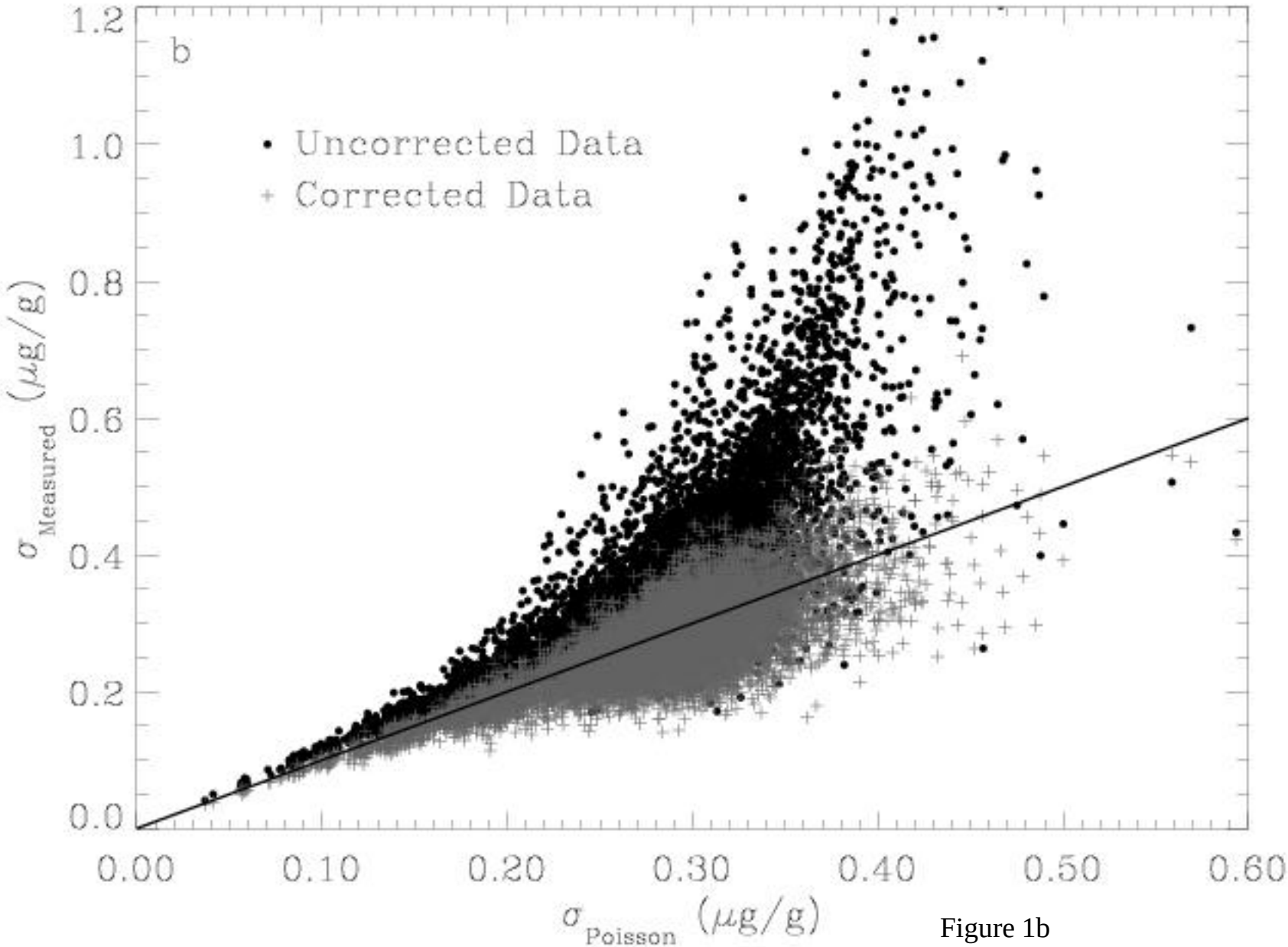
b
Uncorrected Data
Corrected Data
1.2
1.0
0.8
0.6
0.4
0.2
0.0
0.00
0.10
0.20
0.30
0.40
0.50
0.60
σ_{Measured} $(\mu g/g)$
σ_{Poisson} $(\mu g/g)$

Figure 1b

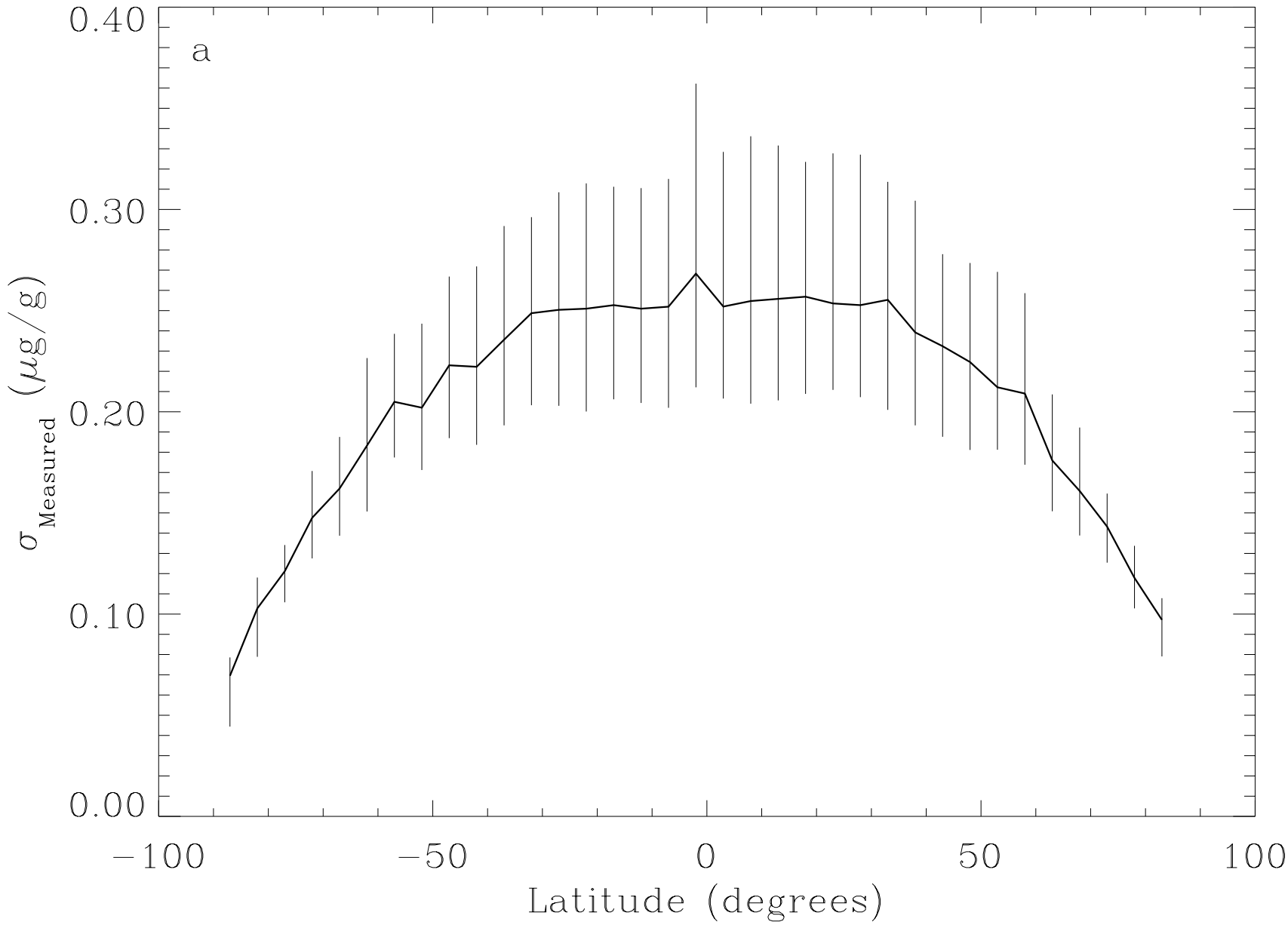
a
0.40
0.30
0.20
0.10
0.00
σ_{Measured} (μg/g)
−100
−50
0
50
100
Latitude (degrees)

Figure 2a

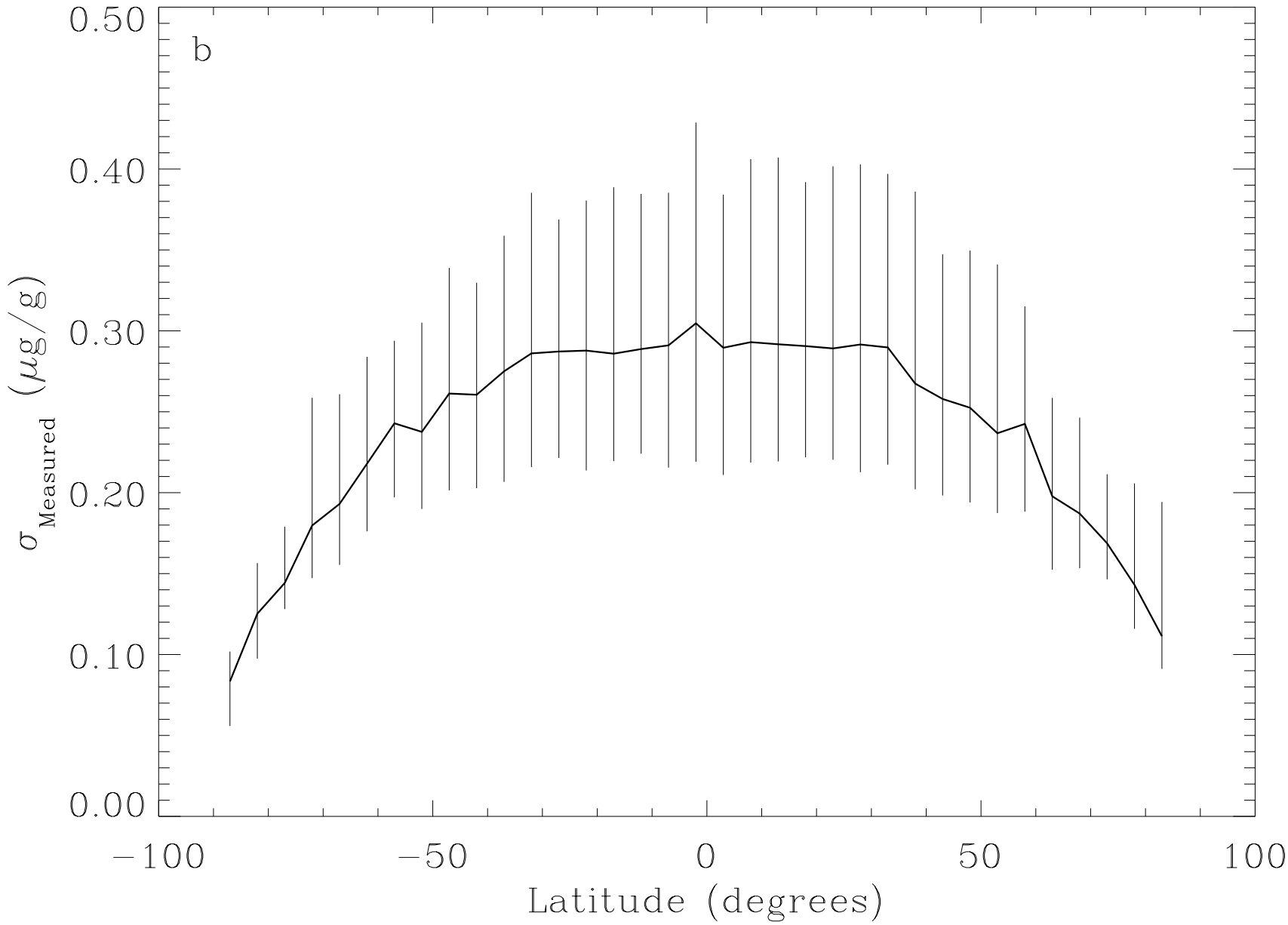
b
0.50
0.40
0.30
0.20
0.10
0.00
σ_{Measured} (μg/g)
−100
−50
0
50
100
Latitude (degrees)

Figure 2b

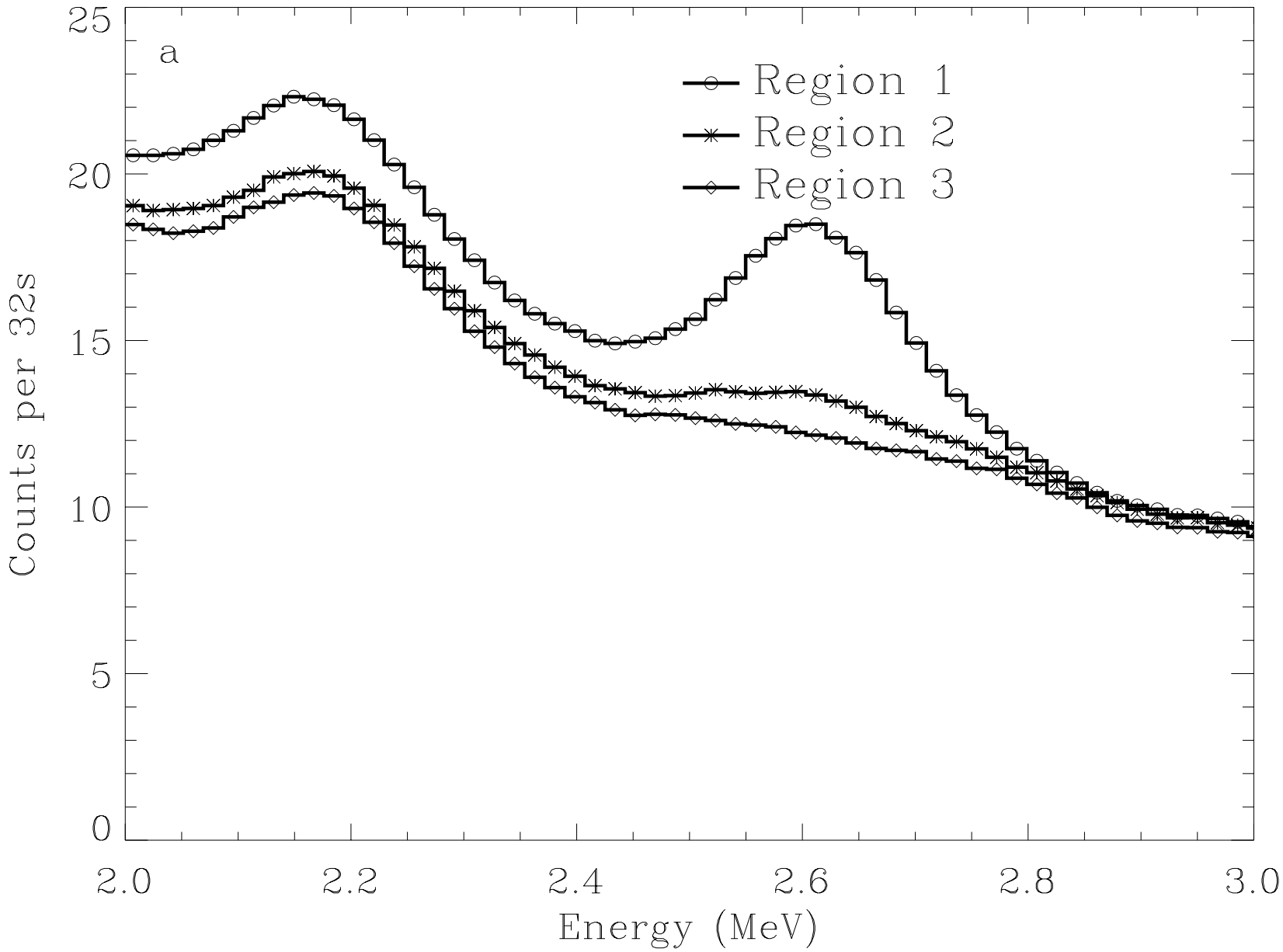
a
Region 1
Region 2
Region 3
Counts per 32s
Energy (MeV)
0
5
10
15
20
25
2.0
2.2
2.4
2.6
2.8
3.0

Figure 3a

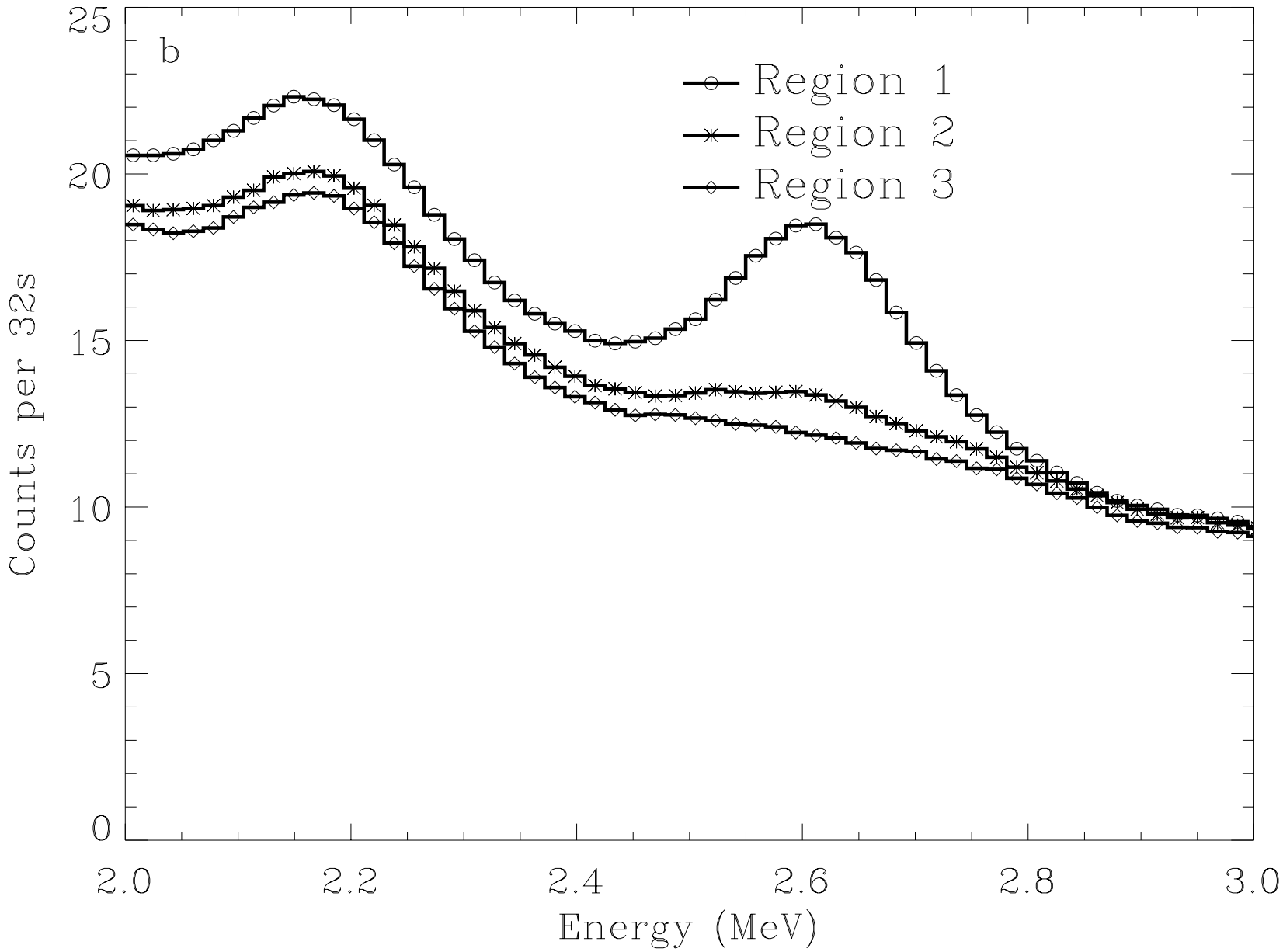
b
Region 1
Region 2
Region 3
Counts per 32s
Energy (MeV)
0
5
10
15
20
25
2.0
2.2
2.4
2.6
2.8
3.0

Figure 3b

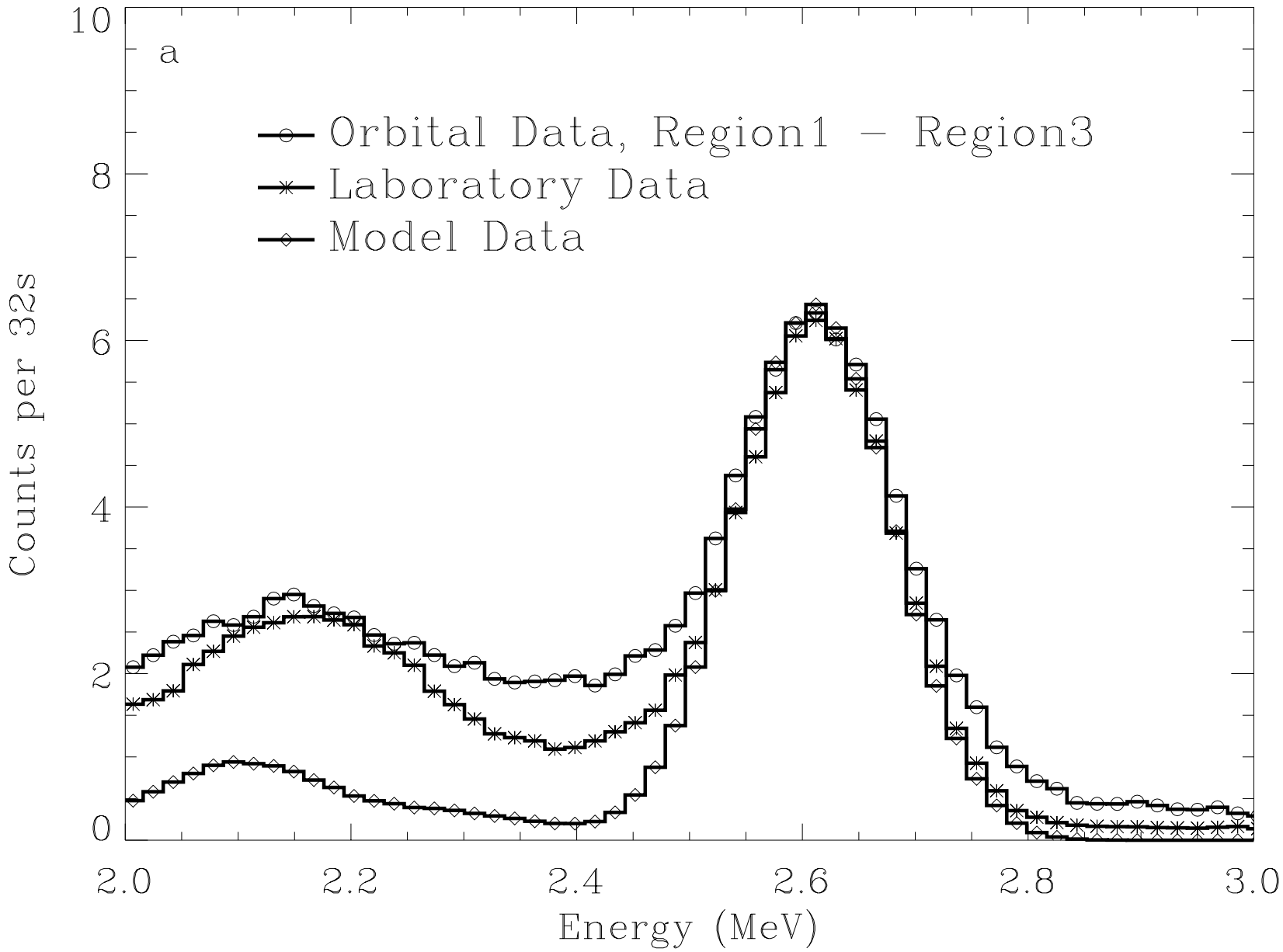
a
Orbital Data, Region1 − Region3
Laboratory Data
Model Data
Counts per 32s
Energy (MeV)
0
2
4
6
8
10
2.0
2.2
2.4
2.6
2.8
3.0

Figure 4a

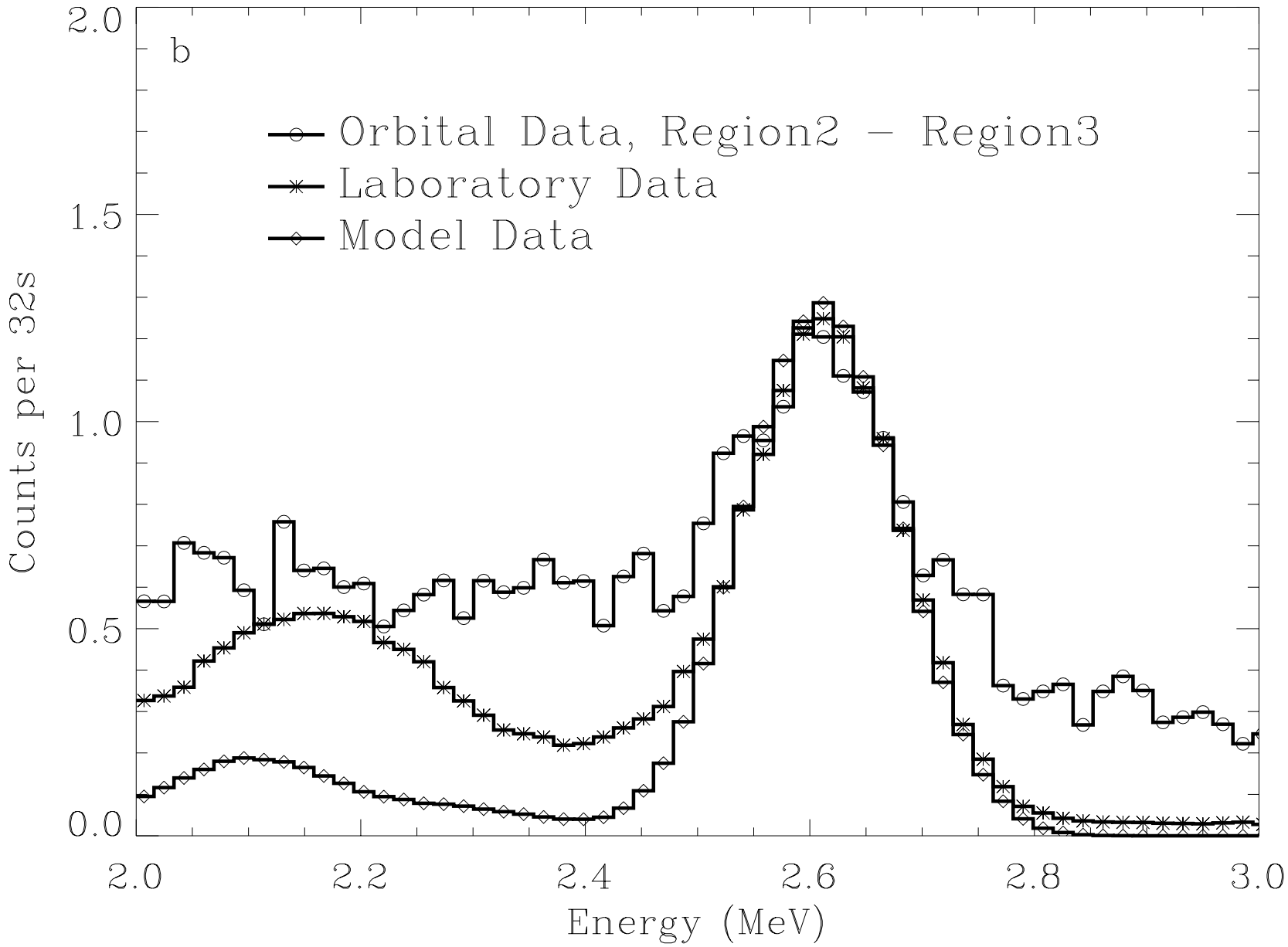
b
Orbital Data, Region2 − Region3
Laboratory Data
Model Data
Counts per 32s
Energy (MeV)
2.0
1.5
1.0
0.5
0.0
2.0
2.2
2.4
2.6
2.8
3.0

Figure 4b

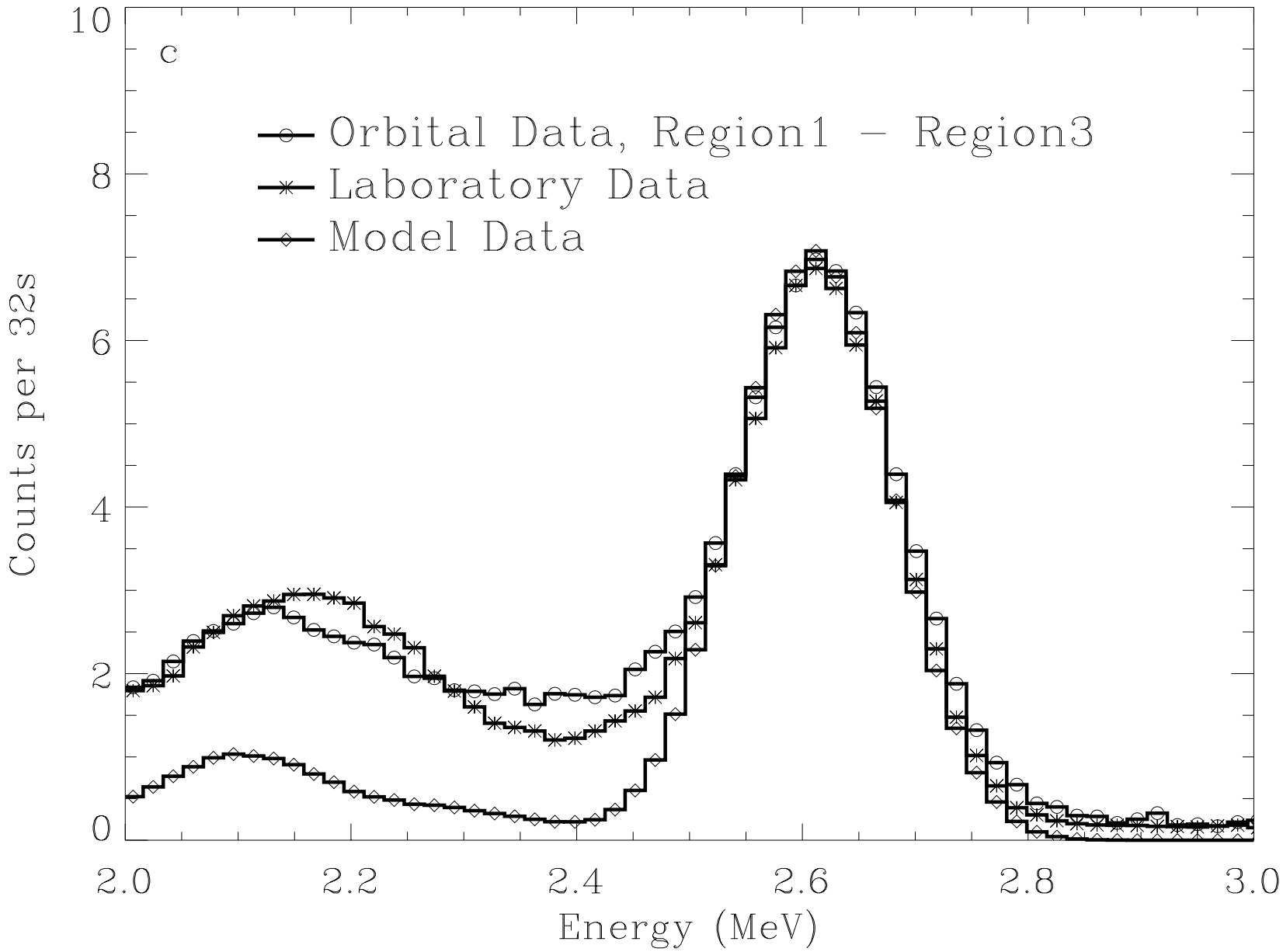
c
Orbital Data, Region1 − Region3
Laboratory Data
Model Data
Counts per 32s
Energy (MeV)
0
2
4
6
8
10
2.0
2.2
2.4
2.6
2.8
3.0

Figure 4c

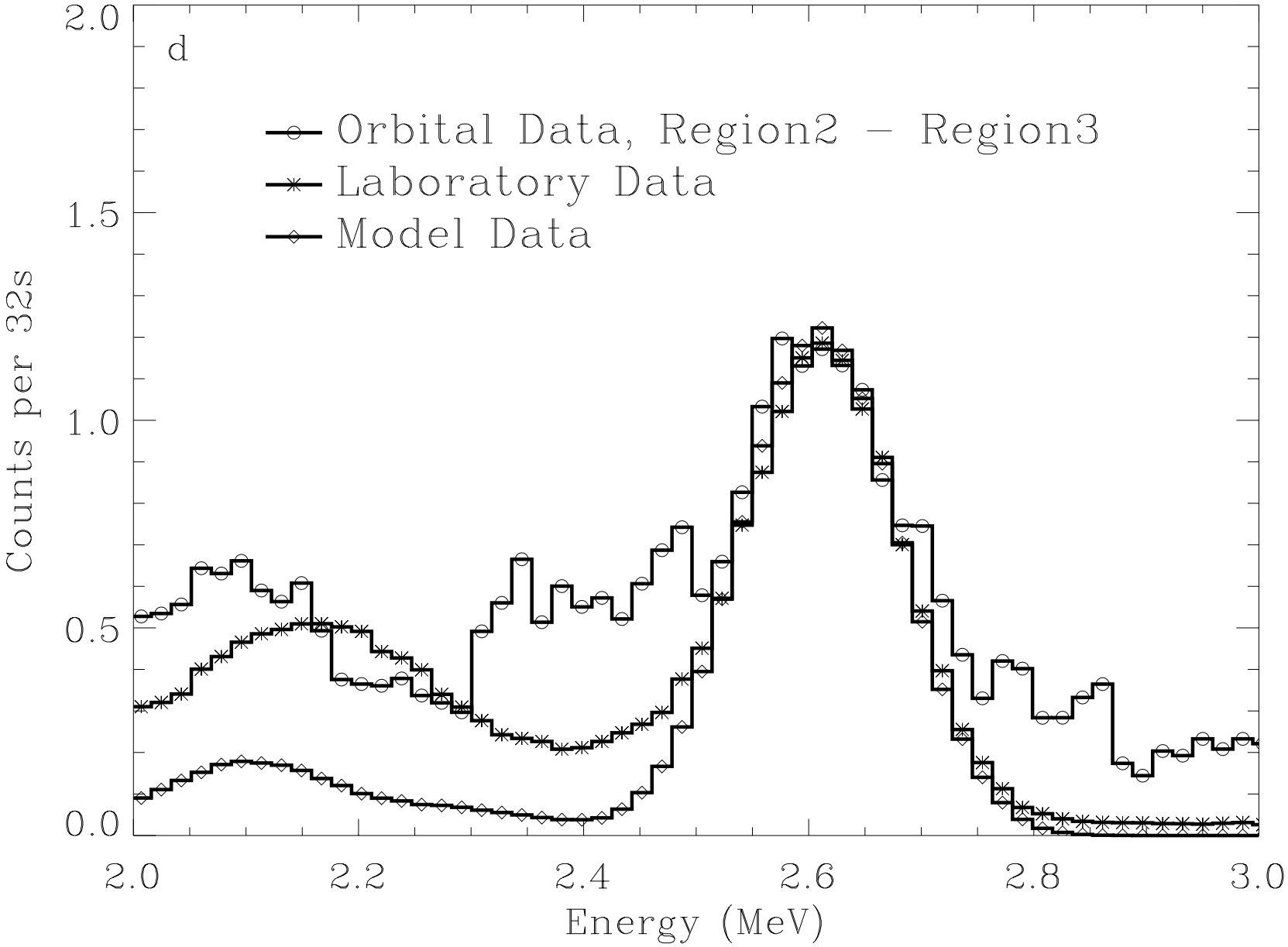
d
Orbital Data, Region2 − Region3
Laboratory Data
Model Data
Counts per 32s
Energy (MeV)
2.0
1.5
1.0
0.5
0.0
2.0
2.2
2.4
2.6
2.8
3.0

Figure 4d

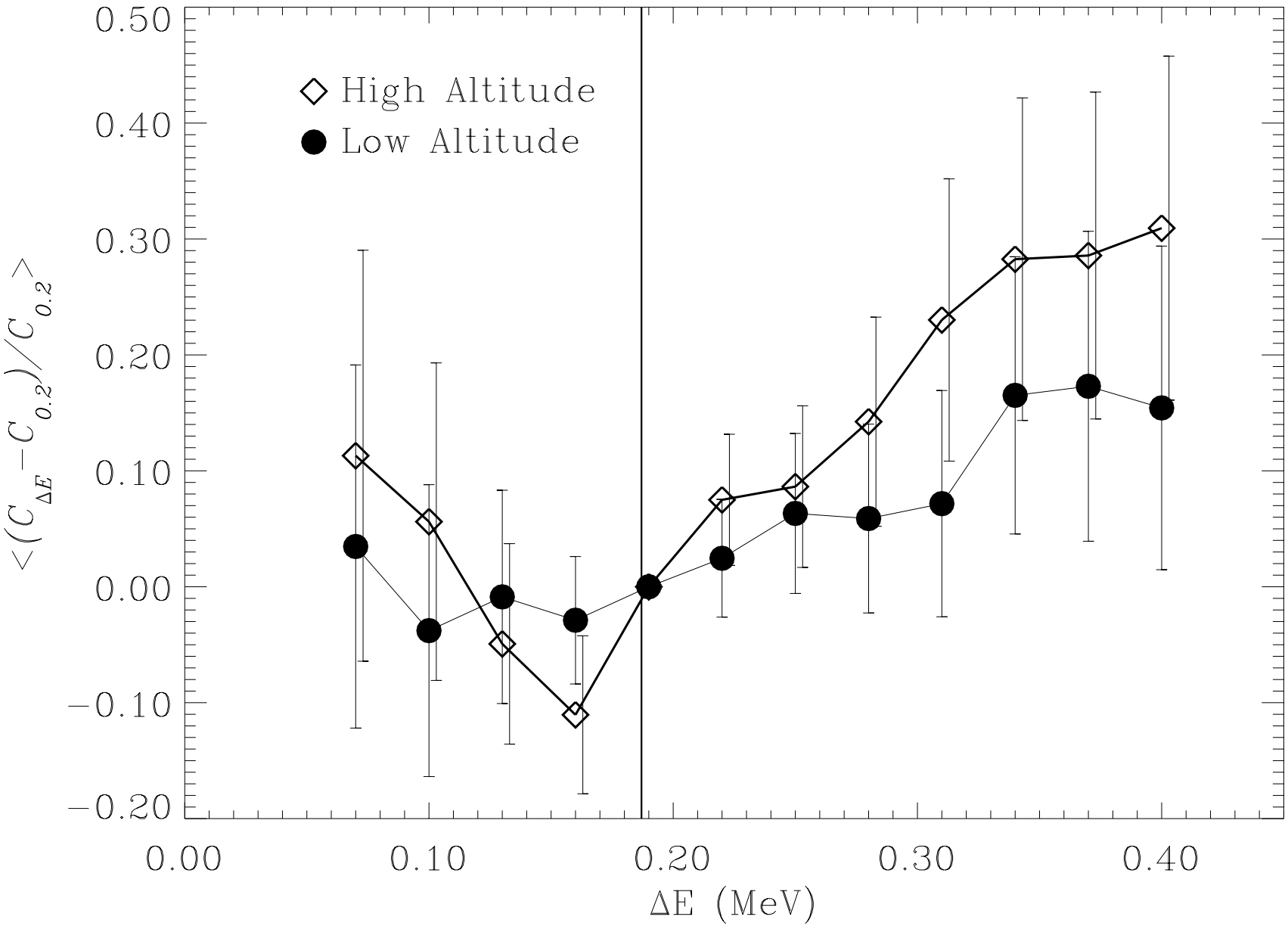
High Altitude
Low Altitude
0.50
0.40
0.30
0.20
0.10
0.00
−0.10
−0.20
0.00
0.10
0.20
0.30
0.40
ΔE (MeV)
$<(C_{\Delta E} - C_{0.2})/C_{0.2}>$

Figure 5

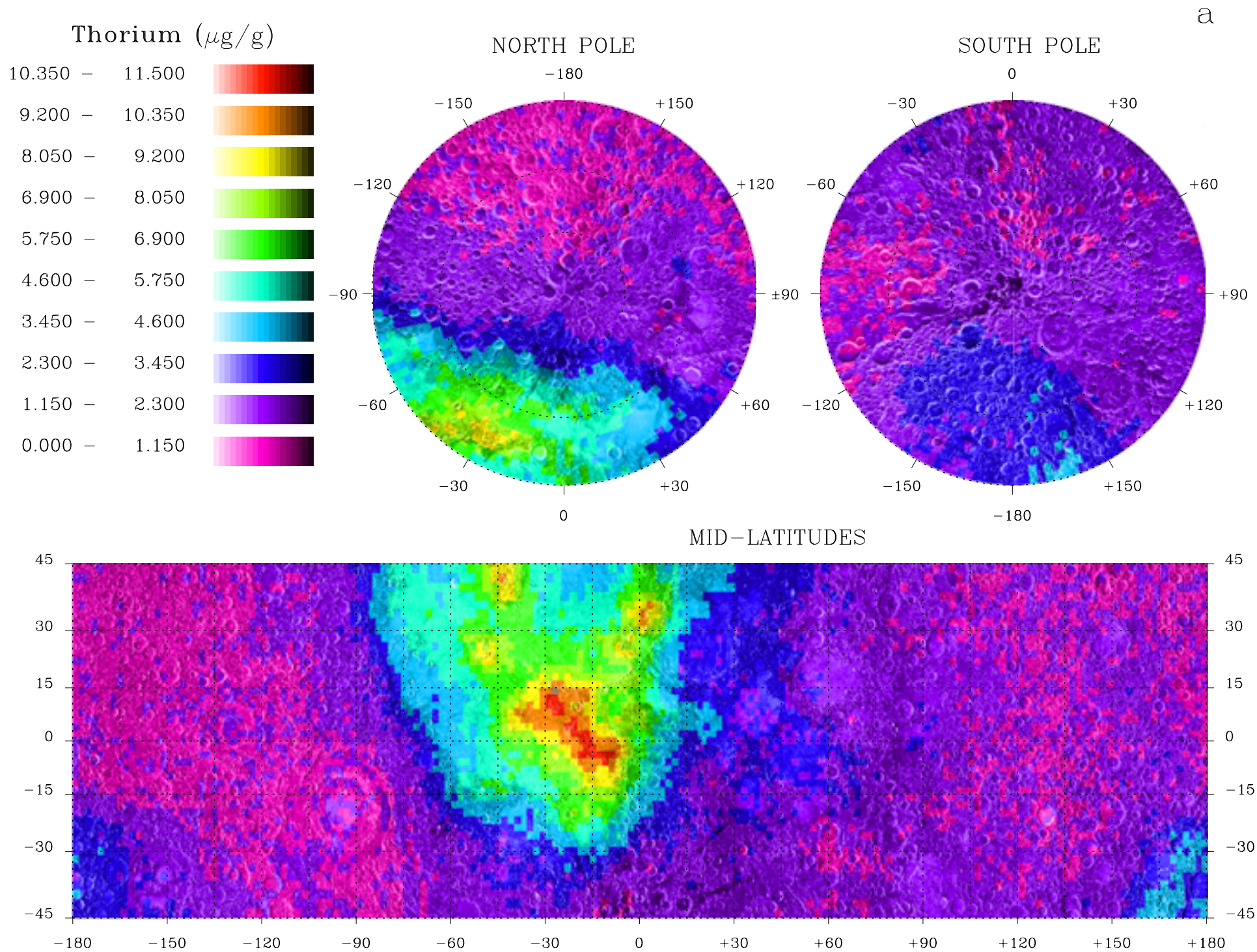
a
Thorium (μg/g)
10.350 – 11.500
9.200 – 10.350
8.050 – 9.200
6.900 – 8.050
5.750 – 6.900
4.600 – 5.750
3.450 – 4.600
2.300 – 3.450
1.150 – 2.300
0.000 – 1.150
NORTH POLE
−180
−150
+150
−120
+120
−90
±90
−60
+60
−30
+30
0
SOUTH POLE
0
−30
+30
−60
+60
+90
−120
+120
−150
+150
−180
MID−LATITUDES
45
30
15
0
−15
−30
−45
−180
−150
−120
−90
−60
−30
0
+30
+60
+90
+120
+150
+180

Plate 1a

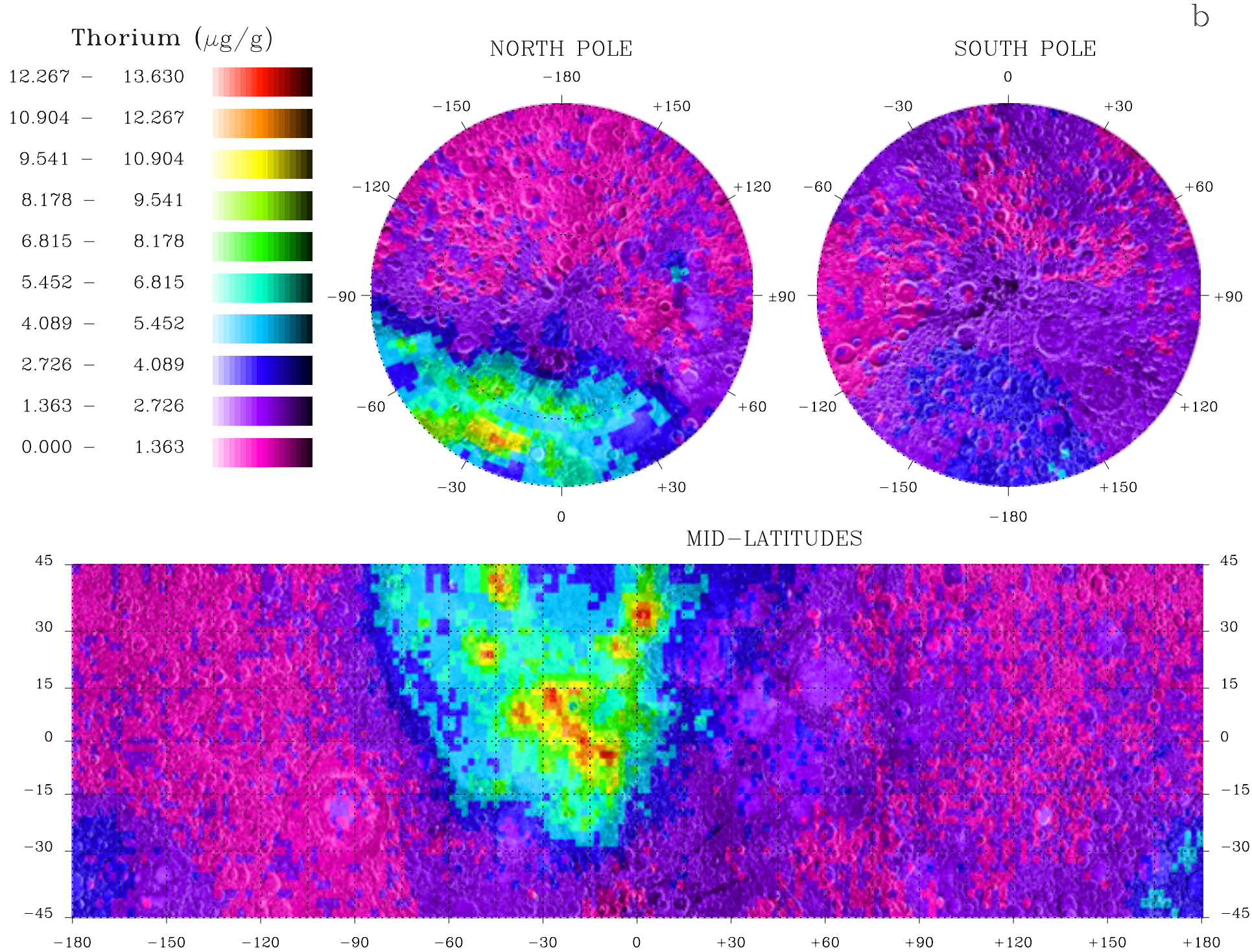
b
Thorium (μg/g)
12.267 – 13.630
10.904 – 12.267
9.541 – 10.904
8.178 – 9.541
6.815 – 8.178
5.452 – 6.815
4.089 – 5.452
2.726 – 4.089
1.363 – 2.726
0.000 – 1.363
NORTH POLE
SOUTH POLE
MID−LATITUDES

Plate 1b

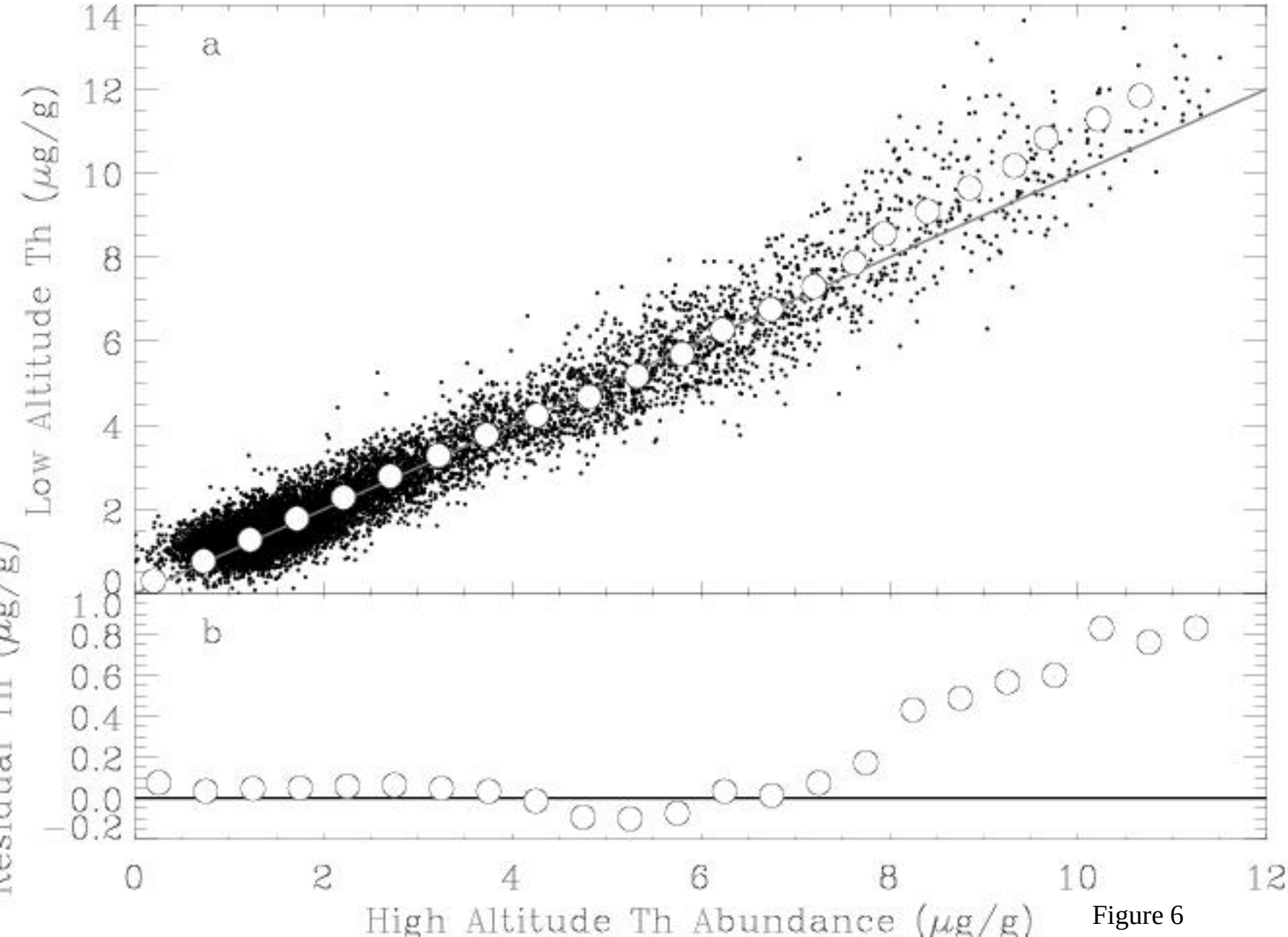
a
b
Low Altitude Th (μg/g)
Residual Th (μg/g)
High Altitude Th Abundance (μg/g)
0
2
4
6
8
10
12
14
0.0
0.2
0.4
0.6
0.8
1.0
−0.2

Figure 6

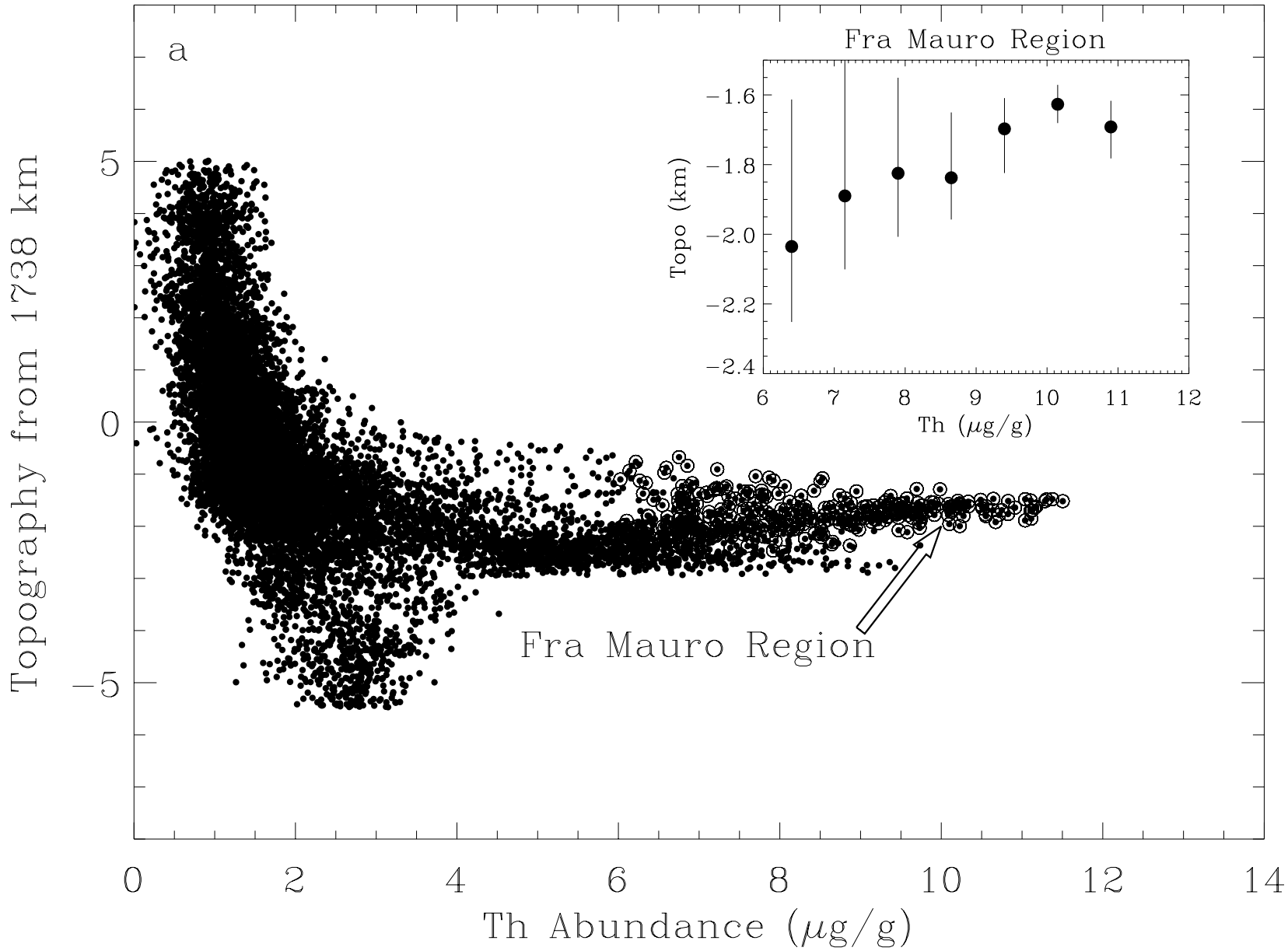
a
Fra Mauro Region
Topo (km)
Th (μg/g)
Topography from 1738 km
Th Abundance (μg/g)
Fra Mauro Region

Figure 7a

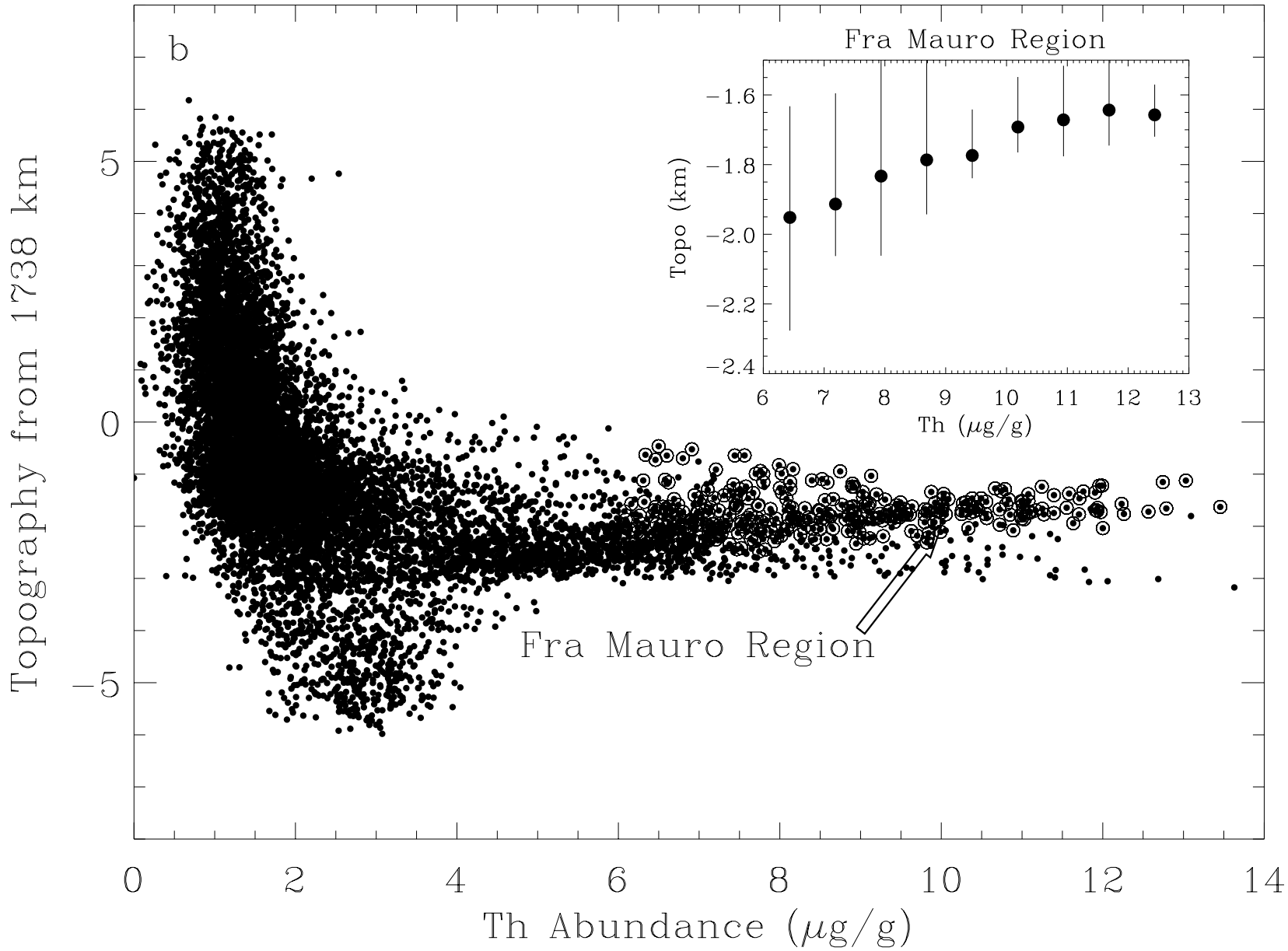
b
Fra Mauro Region
Topo (km)
Th (μg/g)
Topography from 1738 km
Th Abundance (μg/g)
Fra Mauro Region

Figure 7b

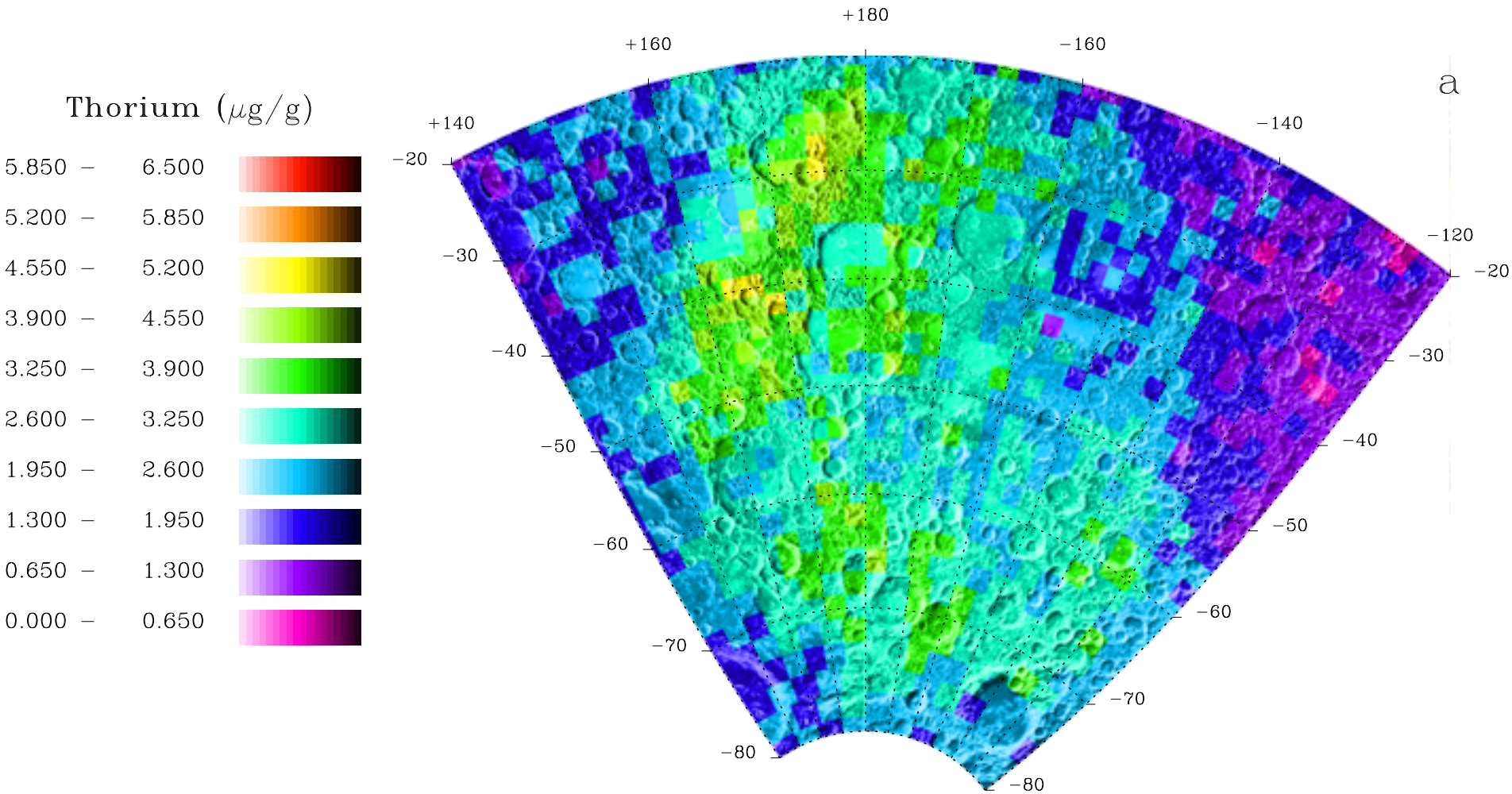
Thorium (μg/g)
5.850 – 6.500
5.200 – 5.850
4.550 – 5.200
3.900 – 4.550
3.250 – 3.900
2.600 – 3.250
1.950 – 2.600
1.300 – 1.950
0.650 – 1.300
0.000 – 0.650
+180
+160
−160
+140
−140
−120
−20
−30
−40
−50
−60
−70
−80
a

Plate 2a

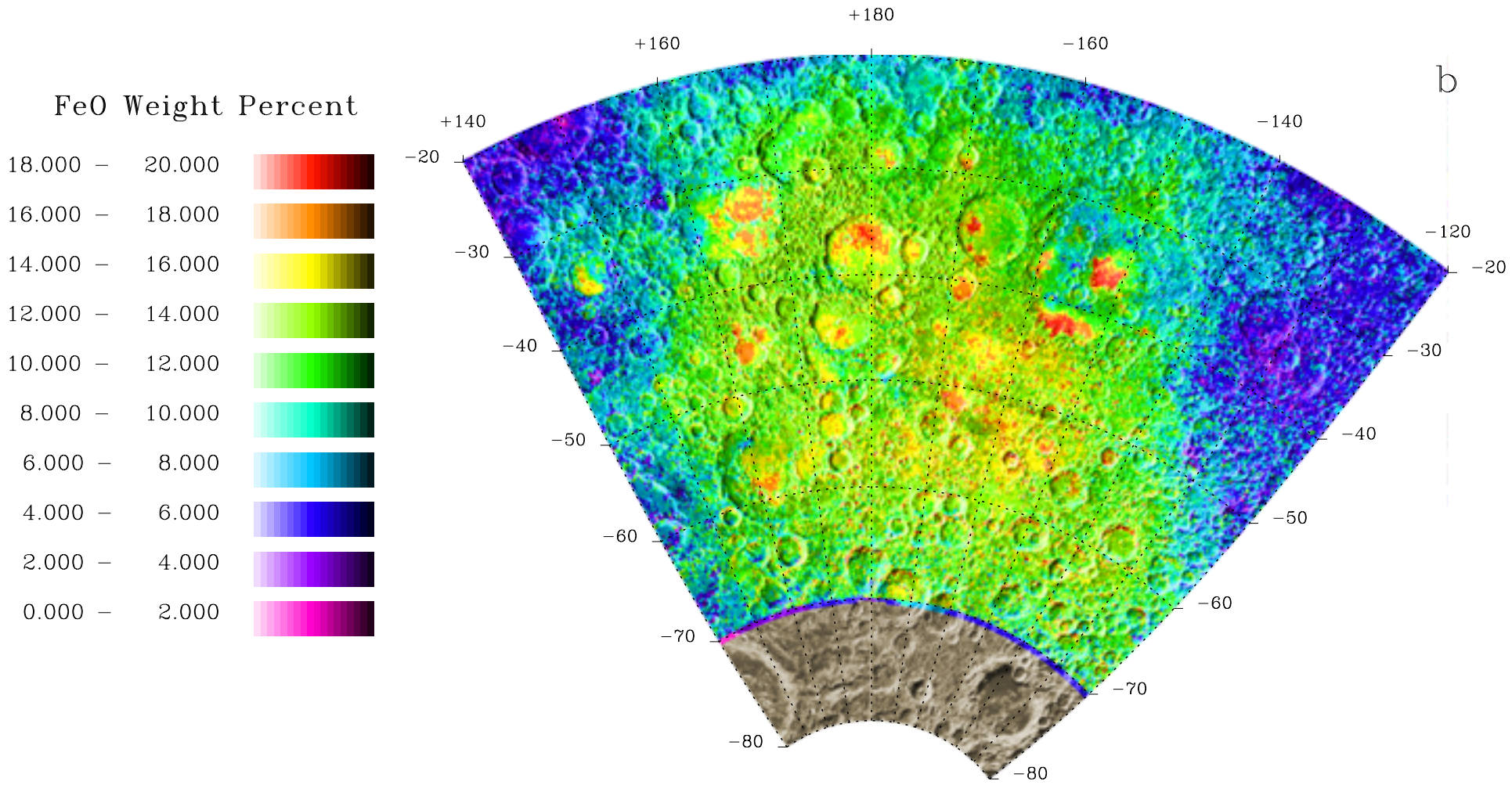
FeO Weight Percent
18.000 – 20.000
16.000 – 18.000
14.000 – 16.000
12.000 – 14.000
10.000 – 12.000
8.000 – 10.000
6.000 – 8.000
4.000 – 6.000
2.000 – 4.000
0.000 – 2.000
b
+180
+160
−160
+140
−140
−120
−20
−30
−40
−50
−60
−70
−80

Plate 2b

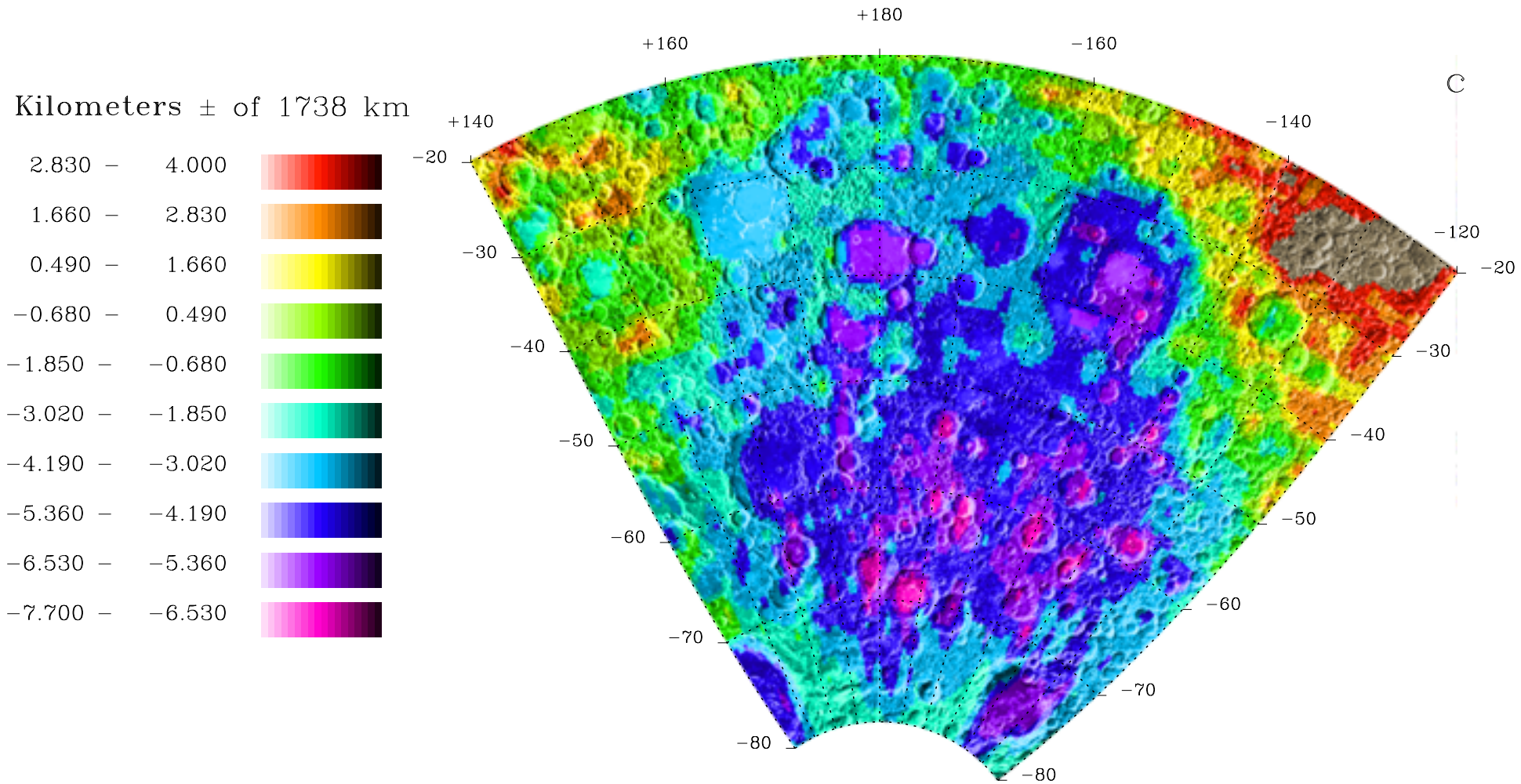
Kilometers ± of 1738 km
2.830 – 4.000
1.660 – 2.830
0.490 – 1.660
−0.680 – 0.490
−1.850 – −0.680
−3.020 – −1.850
−4.190 – −3.020
−5.360 – −4.190
−6.530 – −5.360
−7.700 – −6.530
+180
+160
−160
+140
−140
−120
−20
−30
−40
−50
−60
−70
−80
C

Plate 2c

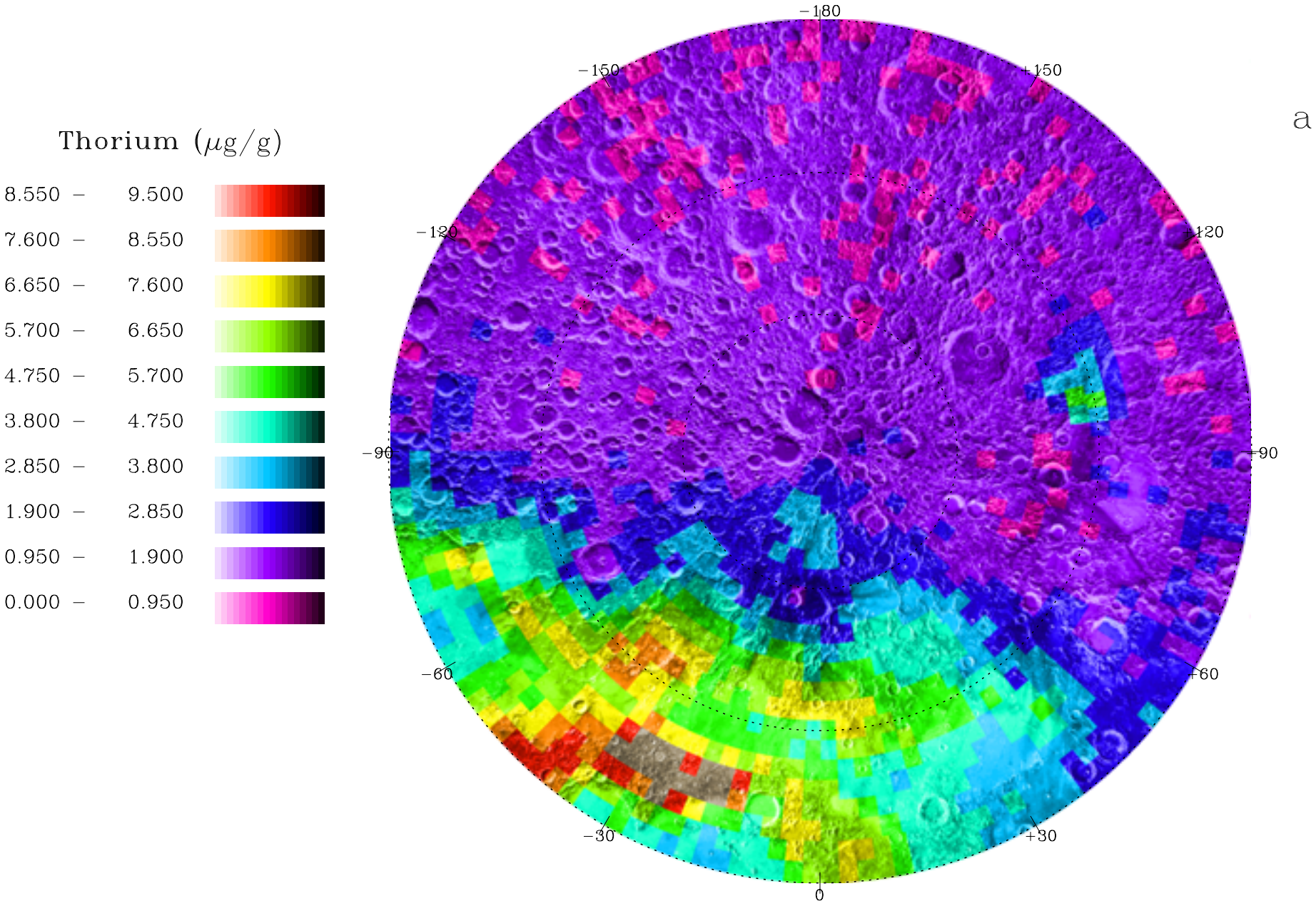
Thorium (μg/g)
8.550 – 9.500
7.600 – 8.550
6.650 – 7.600
5.700 – 6.650
4.750 – 5.700
3.800 – 4.750
2.850 – 3.800
1.900 – 2.850
0.950 – 1.900
0.000 – 0.950
−180
−150
+150
−120
+120
−90
+90
−60
+60
−30
+30
0
a

Plate 3a

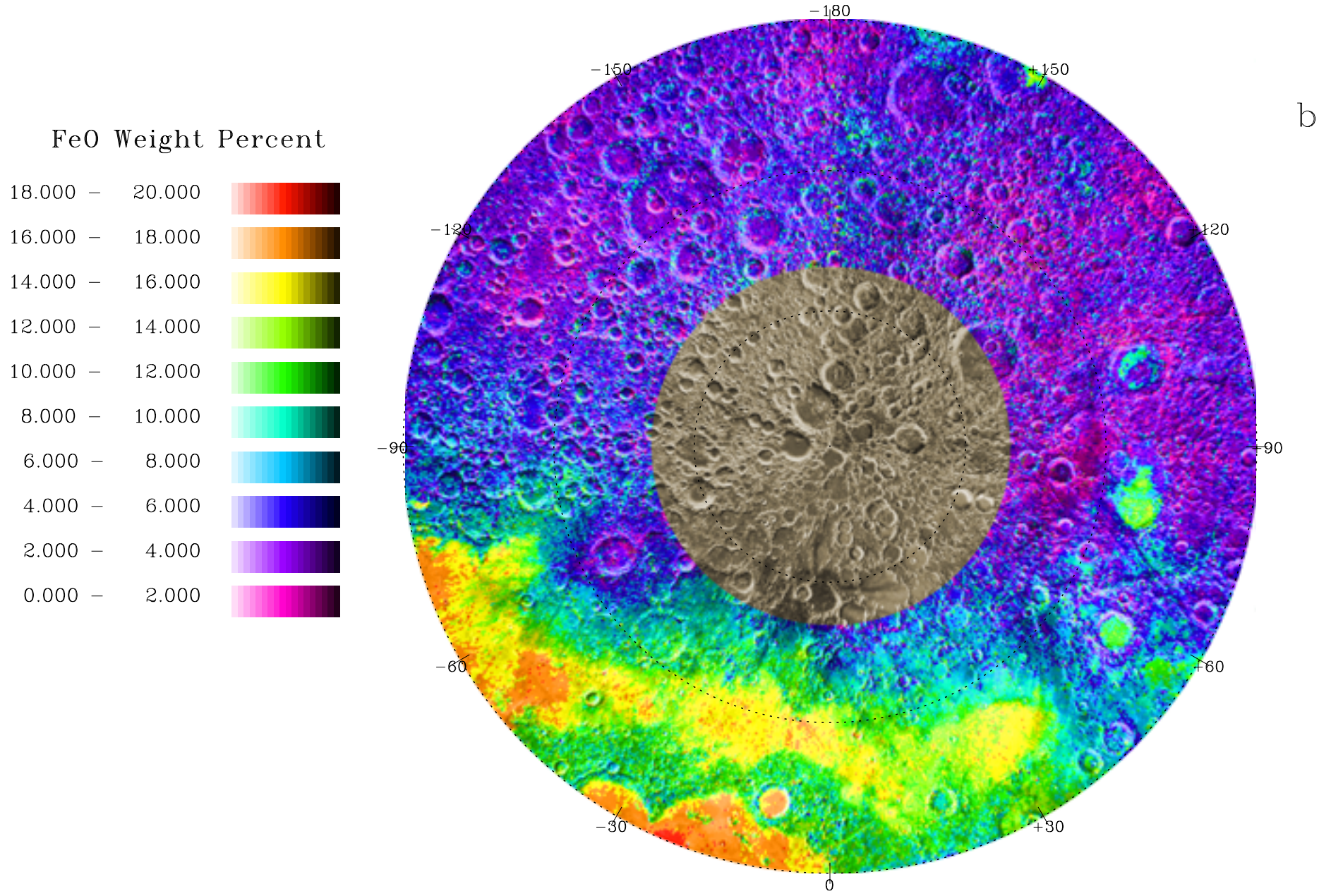
FeO Weight Percent
18.000 – 20.000
16.000 – 18.000
14.000 – 16.000
12.000 – 14.000
10.000 – 12.000
8.000 – 10.000
6.000 – 8.000
4.000 – 6.000
2.000 – 4.000
0.000 – 2.000
b
−180
−150
+150
−120
+120
−90
+90
−60
+60
−30
+30
0

Plate 3b

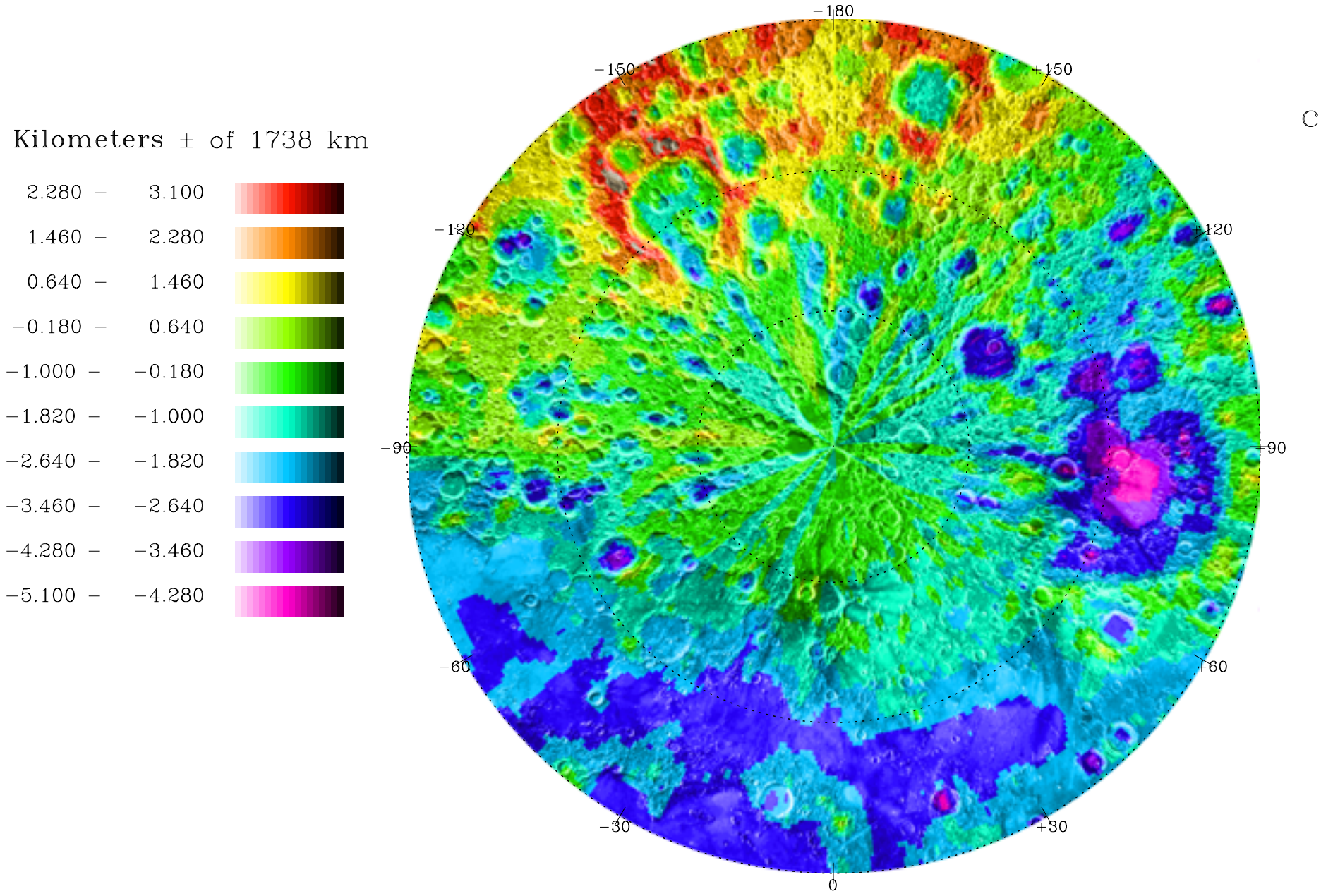
Kilometers ± of 1738 km
2.280 – 3.100
1.460 – 2.280
0.640 – 1.460
−0.180 – 0.640
−1.000 – −0.180
−1.820 – −1.000
−2.640 – −1.820
−3.460 – −2.640
−4.280 – −3.460
−5.100 – −4.280
−180
−150
+150
−120
+120
−90
+90
−60
+60
−30
+30
0
C

Plate 3c

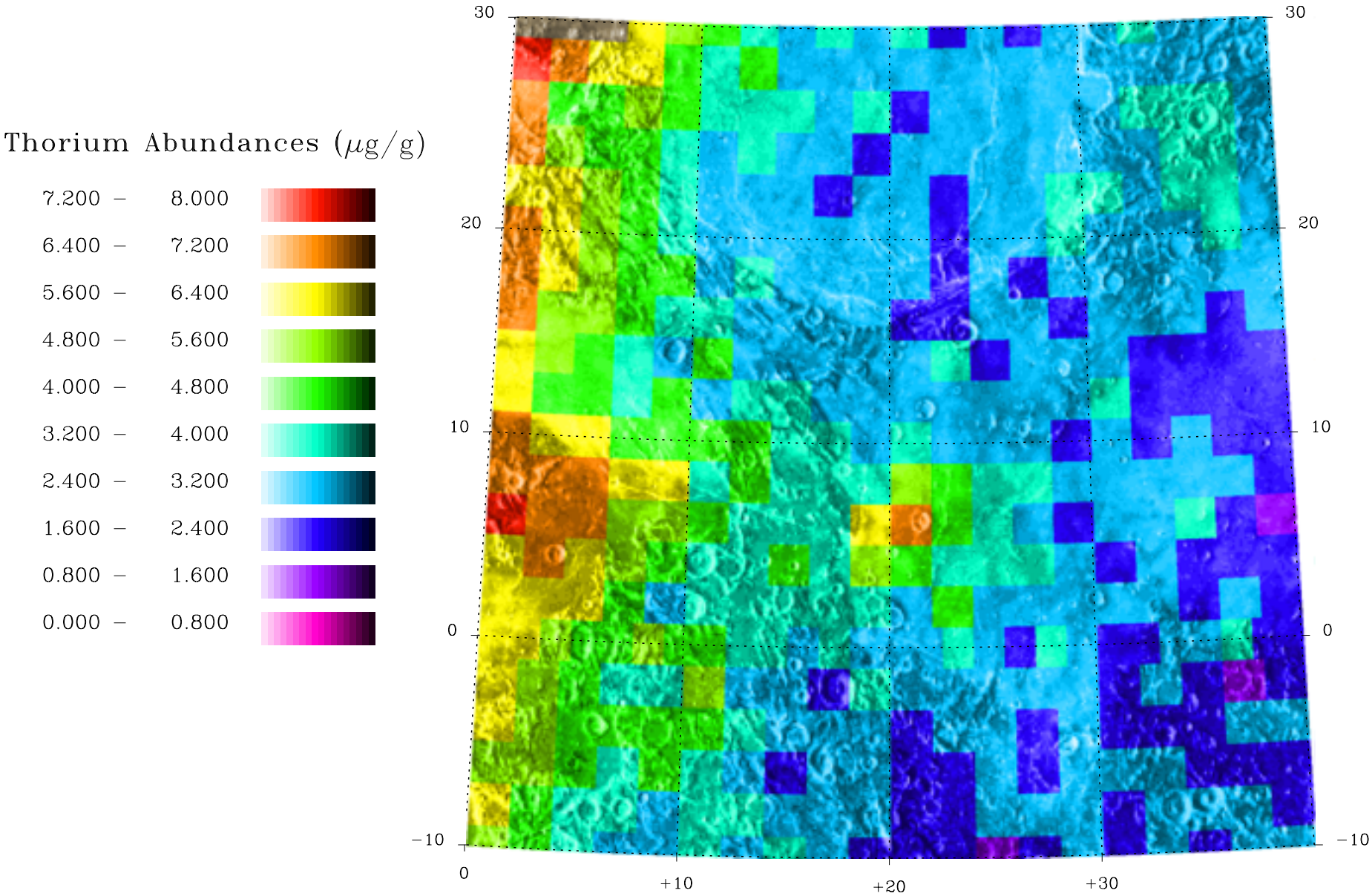
Thorium Abundances (μg/g)
7.200 – 8.000
6.400 – 7.200
5.600 – 6.400
4.800 – 5.600
4.000 – 4.800
3.200 – 4.000
2.400 – 3.200
1.600 – 2.400
0.800 – 1.600
0.000 – 0.800
30
20
10
0
−10
0
+10
+20
+30

Plate 4

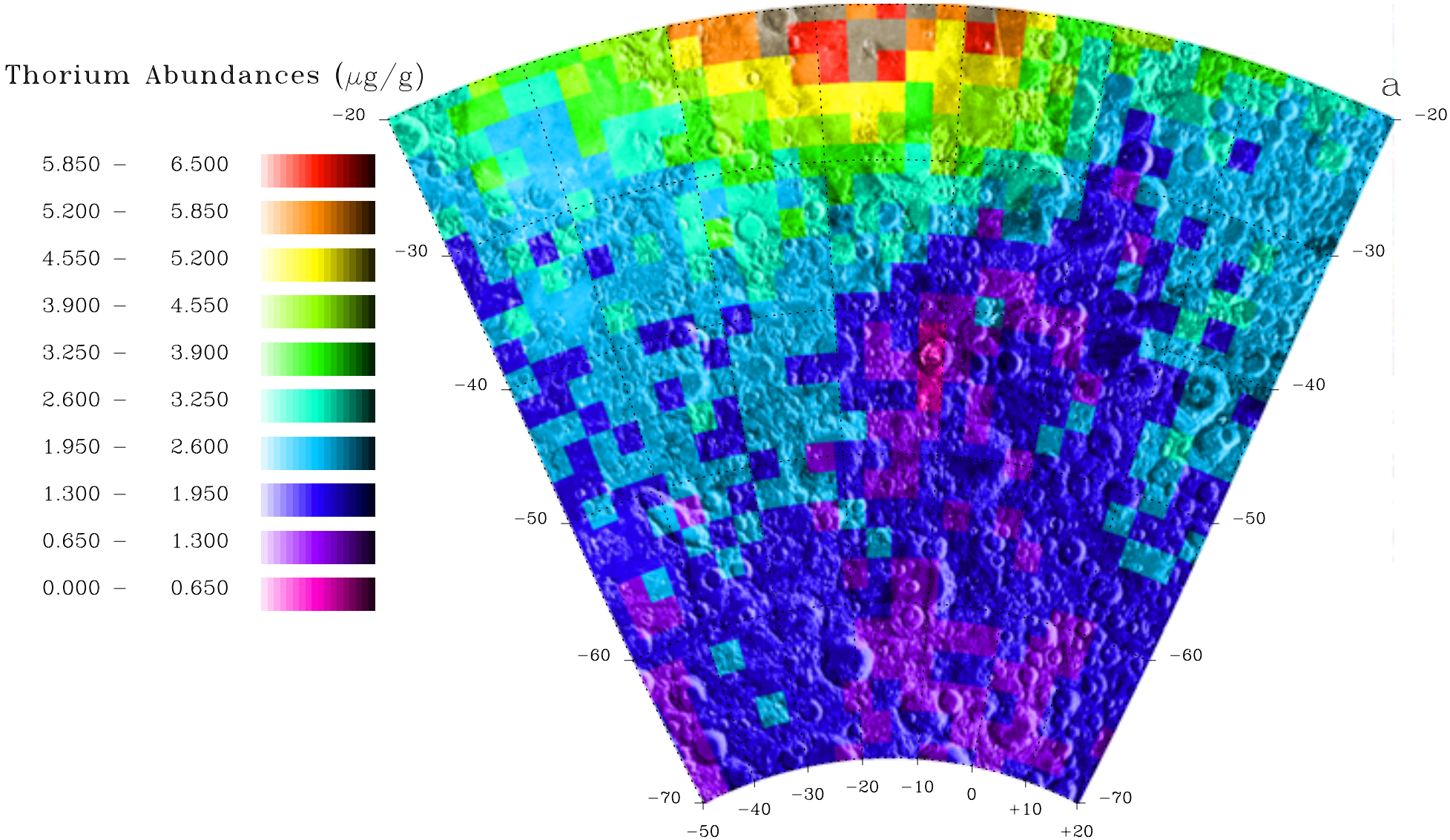
Thorium Abundances (μg/g)
5.850 – 6.500
5.200 – 5.850
4.550 – 5.200
3.900 – 4.550
3.250 – 3.900
2.600 – 3.250
1.950 – 2.600
1.300 – 1.950
0.650 – 1.300
0.000 – 0.650
a
−20
−30
−40
−50
−60
−70
−50
−40
−30
−20
−10
0
+10
+20

Plate 5a

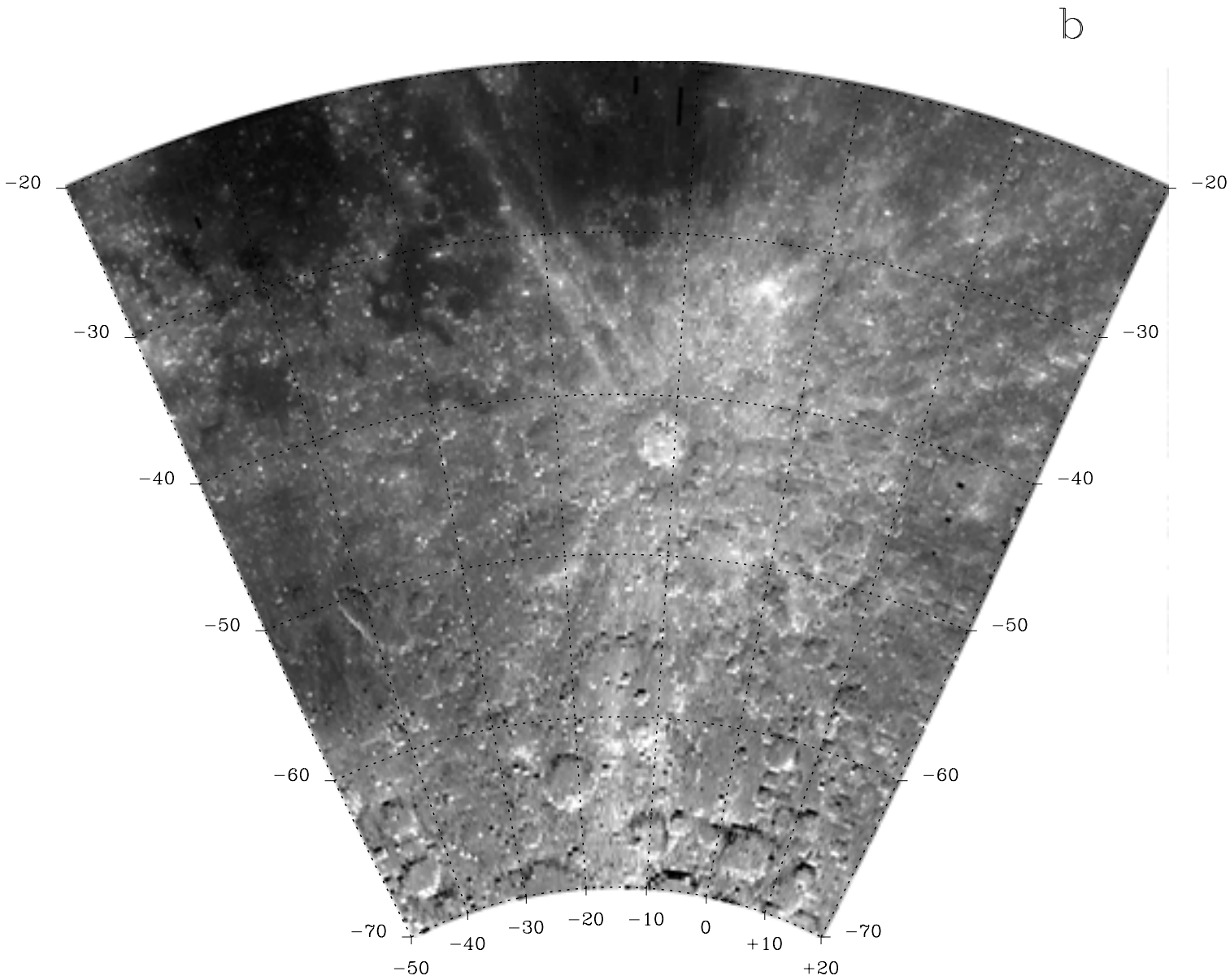

Plate 5b

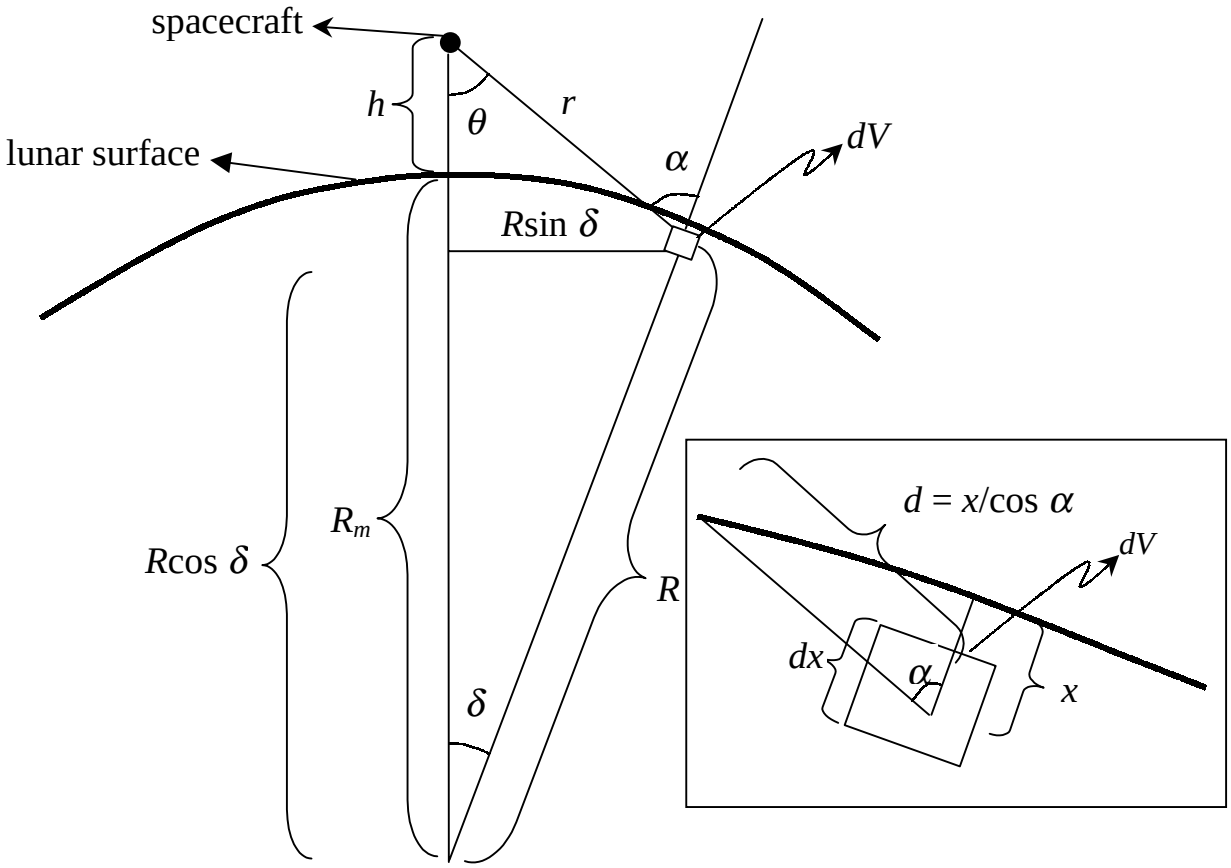
spacecraft
h
θ
r
lunar surface
α
dV
Rsin δ
Rcos δ
R_m
R
δ
d = x/cos α
dV
dx
α
x

Figure A1